9-2010

Charge and Energy Transport in Single Quantum Dot/Organic Hybrid Nanostructures

Kevin Thomas Early
University of Massachusetts Amherst, kearly500@gmail.com

CHARGE AND ENERGY TRANSPORT IN SINGLE QUANTUM DOT/ORGANIC HYBRID NANOSTRUCTURES

A Dissertation Presented

by

KEVIN T. EARLY

Submitted to the Graduate School of the
University of Massachusetts Amherst in partial fulfillment
of the requirements for the degree of

DOCTOR OF PHILOSOPHY

September 2010

Chemistry

CHARGE AND ENERGY TRANSPORT IN SINGLE QUANTUM DOT/ORGANIC HYBRID NANOSTRUCTURES

A Dissertation Presented

by

KEVIN T. EARLY

Approved as to style and content by:

_____
Michael D. Barnes, Chair

_____
Bret Jackson, Member

_____
S. Thayumanavan, Member

_____
Mark Tuominen, Member

_____
Craig Martin, Department Head
Department of Chemistry

DEDICATION

To my fiancé Jillian, my family, and my friends. Thanks for sticking it out.

"And say my glory was I had such friends."

William Butler Yeats

ACKNOWLEDGMENTS

I would like to acknowledge the support and friendship of the members of the Barnes group, without whose help I would not have come this far. I would like to thank the original crew, Michael Odoi, Ruthanne Hassey, and Nathan Hammer, for teaching me the basics and getting me on my feet. I'd like to thank the newer members, Dr. Kevin McCarthy, Dr. Yikuan Wang, Austin Cyphersmith, and Joelle Labastide, for their help along the way. I would also like to acknowledge and thank our collaborators in Prof. Todd Emrick's group, Ravi and Sudeep, for their expertise in synthesis of the materials explored in this work.

I'd like to thank my thesis committee, Profs. Jackson, Thayumanavan, and Tuominen, for their invaluable input over the course of my graduate career, as well as Prof. Venkataraman (DV) and Prof. Emrick for their guidance throughout my stay at UMass. Great thanks go to Dr. Vahid Sandoghdar at ETH Zurich for his hospitality during my research stay there. Lastly, I would like to thank my advisor Mike Barnes for the training, the encouragement, the guidance, and the friendship over the past five years. His unwavering support has brought me to this stage in my career and life, and will propel me on the next one.

ABSTRACT

CHARGE AND ENERGY TRANSPORT IN SINGLE QUANTUM DOT/ORGANIC HYBRID NANOSTRUCTURES

SEPTEMBER 2010

KEVIN T. EARLY, B.S., UNIVERSITY OF CALIFORNIA SAN DIEGO

Ph.D., UNIVERSITY OF MASSACHUSETTS AMHERST

Directed by: Professor Michael D. Barnes

Hybrid quantum dot /organic semiconductor systems are of great interest in optoelectronic and photovoltaic applications, because they combine the robust and tunable optical properties of inorganic semiconductors with the processability of organic thin films. In particular, cadmium selenide (CdSe) quantum dots coordinated with oligo-(phenylene vinylene) ligands have displayed a number of hybrid optical properties that make them particularly well-suited to these applications. When probed on an individual particle level, these so-called CdSe-OPV nanostructures display a number of surprising photophysical characteristics, including strong quenching of fluorescence from coordinating ligands, enhanced emission from the CdSe quantum dot core, suppression of fluorescence intermittency, and photon antibunching, all of which make them attractive in the applications described above. By correlating fluorescence properties with atomic force microscopy, the effects of ligands on quantum dot luminescence are elucidated.

In addition, recent studies on individual CdSe-OPV nanostructures have revealed a strong electronic coupling between the coordinating ligands and the nanocrystal core. These studies have shown that excitations in the organic ligands can strongly affect the electronic properties of the quantum dot, leading to linearly polarized optical transitions

(both in *absorption* and *emission*) and polarization-modulated shifts in band edge emission frequency. These polarization effects suggest exciting new uses for these nanostructures in applications that demand the robust optical properties of quantum dots combined with polarization-switchable control of photon emission.

TABLE OF CONTENTS

Page

LIST OF FIGURES

CHAPTER 1

BACKGROUND ON CdSe-OPV HYBRID NANOSTRUCTURES

1.1 Nanostructured Materials for Thin Film Devices

In the quest for high-efficiency, flexible energy-harvesting devices, nanostructured materials have been targeted because of the ability to specifically tailor domains on the order of the exciton diffusion length. In this regime recombination of charge carriers is greatly suppressed, leading to enhanced device efficiency. Several approaches to this tailoring have been explored, including the incorporation of diblock copolymers and nanocrystalline domains. In all cases, the interface between domains is a critical aspect of device performance. These interfaces often act as bottlenecks to charge separation, resulting in charge trapping and overall device charging. Therefore, understanding the nature of these interfaces is a crucial step in controlling and enhancing device output.

Bulk heterojunction devices have been explored as a means of intimately mixing hole and electron transport layers. In these devices the photosensitizing layer and charge transport layers are interdigitated in continuous domains, maximizing the surface area between layers and minimizing the distance charge carriers must diffuse to be split and carried away as current in a circuit. Diblock copolymers are capable of forming such domains with length dimensions that are sub-exciton diffusion length, increasing device efficiency and suppressing radiative and non-radiative recombination. These techniques have been used, for example, to improve interfacial contact in regio-regular polythiophene/fullerene devices.[1] Semiconducting organic polymers also possess appealing characteristics for charge separation. Poly[2-methoxy-5-(2'-ethyl-hexyloxy)-

1,4-phenylenevinylene] (MEH-PPV) polymers are attractive candidates, due to their ease of processing and the ability to vary side chain functionalities. In this way, tunability of the HOMO-LUMO gap and packing ability of the absorbing polymer allows for control of both of the factors mentioned above. Power conversion efficiencies based on these polymers have exceeded 2.5% and continue to be investigated.[2]

However, devices based on semiconducting polymers are not without drawbacks. The long-term stability of organic photovoltaics suffers in comparison to inorganic semiconductor devices. Power conversion efficiencies in all-organic photovoltaic devices suffer in comparison to monocrystalline silicon, polycrystalline CdTe, and copper/ indium/ gallium/ selenide (CIGS)-based devices, largely due to the small exciton diffusion lengths inherent to semiconductor organic absorbers (~4-20 nm).[3, 4] For these reasons, alternative materials have been explored to bolster power conversion efficiencies. In particular, semiconductor quantum dots have been explored as photosensitizers in next-generation photovoltaic systems.[5, 6] These materials meet the requirements for photophysical characteristics, stability, and processibility in photovoltaic applications.

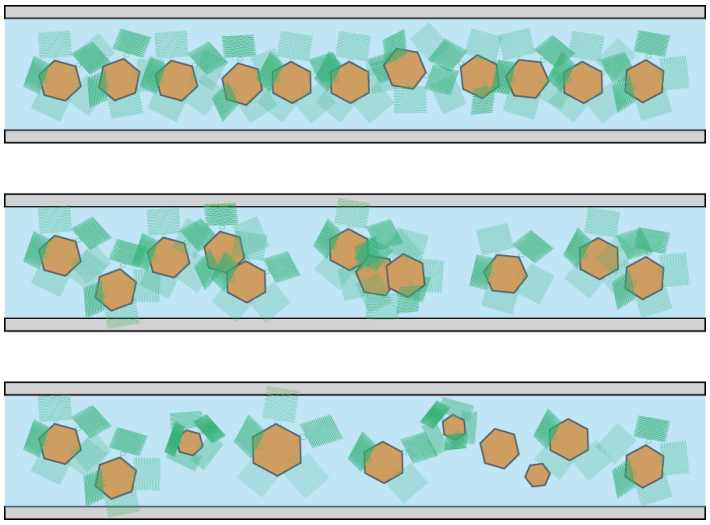

Figure 1. Schematic of nanocrystal-based photovoltaic devices. (Top) Uniformly deposited, homogeneous layer. (Mid) Non-uniform, homogeneous layer. (Bottom) Non-uniform, inhomogeneous nanocrystals.

Inherent heterogeneities in nanocrystal morphology (shape, radius, etc.) during the QD synthesis process can vastly alter their photophysical behavior (more on this below). When studied as an ensemble, individual particle behaviors are almost completely obscured. Figure 1 illustrates this problem. In hybrid photovoltaic devices incorporating nanocrystals and charge-carrier polymers, charge mobility devices can depend on deposition characteristics (top and middle) and nanocrystal heterogeneity (bottom). In order to fully understand the chemical physics of devices composed of such materials, a particle-by-particle approach is required. In the following, chemical microscopy techniques are used to study the behaviors of single nanostructures composed of quantum dot- and organic polymer components. By studying single hybrid nanostructures, we avoid the averaging effects associated with assaying a large ensemble of molecules (i.e. photoluminescence experiments on ~10^{23} molecules in a fluorescence cuvette or thin film). While these experiments only practically allow for observations on a few hundreds of molecules, statistical treatments can then be used to relate single particle behaviors to their bulk analogs. In this way, it is possible to disentangle properties and limitations arising single particle behavior and those arising from extrinsic device parameters.

1.2 Background on Quantum Dots

Colloidal semiconductor quantum dots (QDs) are nanometer-sized crystals composed of hundreds or thousands of atoms that exhibit characteristics in between bulk semiconductors and small atomic clusters. Colloidal QDs, in constrast to epitaxially-grown QDs, are formed by seeded nucleation in solution without need for a crystalline surface and form suspended, quasi-spherical particles. They are widely used today as easily-synthesized,[7-9] tunable fluorophores in a number of applications. Due to the quantum confinement of exciton wavefunctions imposed by nanocrystal diameters less than the Bohr exciton radius (~13 nm for CdSe), the band gap energy in QDs can be tuned simply by controlling crystal growth in solution. This has spurred the use of QDs in photovoltaic absorbing layers as a means of maximizing coverage of the entire visible and near-IR solar spectrum. To passivate and protect the surfaces of QDs from oxidizing agents, organic capping agents such as tri-*n*-octylphosphine oxide (TOPO) and hexadecylamine (HDA) are introduced during the synthesis.

The quantum-confined exciton states in CdSe nanocrystals are decribed by solutions to the particle-on-a-sphere problem, with

$$V(r) = V, \quad 0 < r < a,$$
$$V(r) = \infty, \quad r > a.$$

where *a* corresponds to the nanocrystal radius. Solutions to this system for both electrons and holes are products of the spherical Bessel functions and spherical harmonics

$$\psi_{nlm}(r,\theta,\phi) = R_{nl}(r)Y_l^m(\theta,\phi).$$

For the band edge electron state, solutions take the form[10-12]

$$\psi_\alpha(r) = \sqrt{\frac{2}{a}}\frac{\sin(\pi r/a)}{r}Y_0^0(\theta,\phi)|S\alpha\rangle$$

with eigenvalues

$$E_{1Se} = \frac{\hbar^2\pi^2}{2m_e a^2}.$$

Above, m_e is mass of the electron, and $|S\alpha\rangle$ are the conduction band electron Bloch functions $|S\alpha\rangle = \sqrt{8}\cos(2\pi x/d)\cos(2\pi y/d)\cos(2\pi z/d)|\alpha\rangle$ ($\alpha = \uparrow$ or $\downarrow$). These energies represent corrections to the bulk CdSe band-edge electronic states.

The wavefunctions for hole states are more complex due to their four-fold degeneracy (spin z-axis angular momentum projections M = ± 3/2, ± 1/2). Their general form is given by

$$\psi_M(r) = 2\sum_{l=0,2} R_l(r) \sum_{m+\mu=M} \begin{pmatrix} 3/2 & l & 3/2 \\ \mu & m & -M \end{pmatrix} Y_l^m(\theta,\phi)u_\mu,$$

where the term in brackets are the Wigner 3*j* symbols. The u_m are the valence band Bloch functions (m = ± 3/2, ± 1/2)

$$\begin{aligned}
u_{3/2} &= \frac{1}{\sqrt{2}}(X+iY)\uparrow, \\
u_{-3/2} &= \frac{i}{\sqrt{2}}(X-iY)\downarrow, \\
u_{1/2} &= \frac{i}{\sqrt{6}}\left[(X+iY)\downarrow -2Z\uparrow\right], \\
u_{1/2} &= \frac{1}{\sqrt{6}}\left[(X-iY)\uparrow -2Z\downarrow\right].
\end{aligned}$$

where X,Y, and Z are given by

$$\begin{aligned}
X &= \sqrt{8}\sin(2\pi x/d)\cos(2\pi y/d)\cos(2\pi z/d), \\
Y &= \sqrt{8}\cos(2\pi x/d)\sin(2\pi y/d)\cos(2\pi z/d), \\
Z &= \sqrt{8}\cos(2\pi x/d)\cos(2\pi y/d)\sin(2\pi z/d).
\end{aligned}$$

Details of the hole wavefunctions are considered in more detail in the perturbation calculations detailed in chapter 5. Eigenvalues for holes are given by

$$E(\beta) = \frac{\hbar^2 \varphi^2(\beta)}{2 m_{hh} a^2},$$

where m_{hh} is the heavy hole effective mass, and j is a function of ratio of the effective masses of the light- to heavy holes. Individual electron and hole states are labeled by nL_M, where n,L,m are principal quantum number, orbital angular momentum (specified by S,P,D, etc.), and spin angular momentum. Conventionally, the band edge exciton states are labeled $1S_e$ (where the electron s = ± 1/2 is implied) and $1S_{3/2}$ for holes.

The oscillator strength of the band-edge transition is described by

$$P = \left| \left\langle 1S_e \left| e\hat{p} \right| 1S_{3/2} \right\rangle \right|^2,$$

where p is the momentum operator, and e is the charge constant. The electronic wavefunction $\left|1S_e\right\rangle$ factors into an envelope part and a Bloch part:

$$\left|1S_e\right\rangle = \left|S\right\rangle \left|\alpha, \beta\right\rangle.$$

α and β refer to the electron spin state. Similarly, $\left|1S_{3/2}\right\rangle$ factors into

$$\left|1S_{3/2}\right\rangle = \left|S\right\rangle \cdot u_M,$$

where the u_M are the Bloch functions for the hole states and contain components along X, Y, and Z (given above). The overlap integrals for the envelope functions are calculated analytically, and the spin integrals determine the selection rules. The optically allowed transitions are shown in figure 2(a). The exciton states with total angular momentum F = (α,β + M) = ±2 are optically passive, because they are separated by two units of angular momentum. The allowed transitions are coupled by emission and absorption of left, right, and linearly polarized photons (denoted by σ^+, σ^-, and z) and correspond to specific

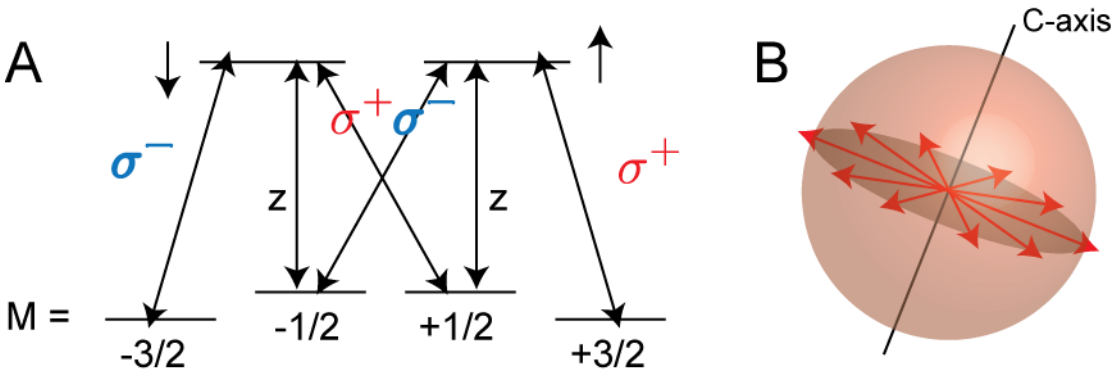

Figure 2. (a) Optical transitions involved in the band-edge states for CdSe. M refers to the hole spin, ↑ and ↓ denote electron spin, and $\sigma^{+(-)}$ refer to left and right circularly polarized light, and z refers to linearly polarized transitions. (b) Illustration of the "2D degenerate dipole" in a CdSe QD.

directions in the crystal relative to c-axis. The $\langle S=\downarrow|\hat{p}|M=-1/2\rangle$ and $\langle S=\uparrow|\hat{p}|M=+1/2\rangle$ matrix elements are polarized along the z-axis, while the $\langle S=\downarrow|\hat{p}|M=+1/2\rangle$ and $\langle S=\uparrow|\hat{p}|M=-1/2\rangle$ transitions involve the $X\pm iY$ hole Bloch functions. This gives rise to complex transition dipole moments for single nanocrystals that are often described as a "2D degenerate dipole,"[13, 14] which forms a disk lying perpendicular to the crystal c-axis (on the "equator" of the nanocrystal). This is shown schematically in fig. 2(b). Experimental manifestations of this will be discussed in Chapter 4.

From the above, it is clear that stronger confinement (smaller *a*) leads to a larger band gap (i.e. exciton recombination energy) in the nanocrystal. This is shown in Figure 3, where the band edge absorption peak ($1S_e - 1S_{3/2}$) at 2.21 eV is labeled by the total angular momentum for the electron and hole states involved in the transition (absorption shown in blue). This is significantly blue-shifted from the bulk CdSe band gap at 1.74 eV.[15] Also shown is the emission spectrum for the same sample excited at 405 nm (3.06 eV). The emission peak occurs at 2.18 eV, with a Stokes shift of 30 meV (grey) from the absorption edge. This Stokes shift is attributed to emission from the F = ±1 states, which lie energetically above the optically forbidden F = ±2 transitions. The narrow emission

peak is evidence of efficient and fast thermal relaxation of hot excitons to the band edge, because emission from any other allowed optical transition ($1P_e - 1P_{3/2}$, for example) is not observed.

Although the internal electronic structure of CdSe quantum dots largely determines the photophysics, the small diameters (~3-10 nm) of colloidal QDs render their surfaces very important, because the surface-to-volume ratio in this size regime is very large. Surface treatments play a large part in QD formation and stabilization in solution, as well as surface protection when removed from solvent.[16] In standard syntheses, Cd and Se precursors are combined in dissolved coordinating TOPO ligands, which allow CdSe crystals to nucleate despite the highly unstable surface geometries. When removed from solvent, the remaining TOPO ligands form an alkane shell which passivates dangling bonds from surface Cd and Se atoms. In cases where higher quantum yield is desirable, additional monolayers of ZnS are grown on the CdSe surface. This shell serves to passivate dangling surface bonds completely, because the lattice parameters are CdSe and ZnS are very similar. In these cases, numerical calculation of exciton wavefunctions must allow for leakage of the electronic

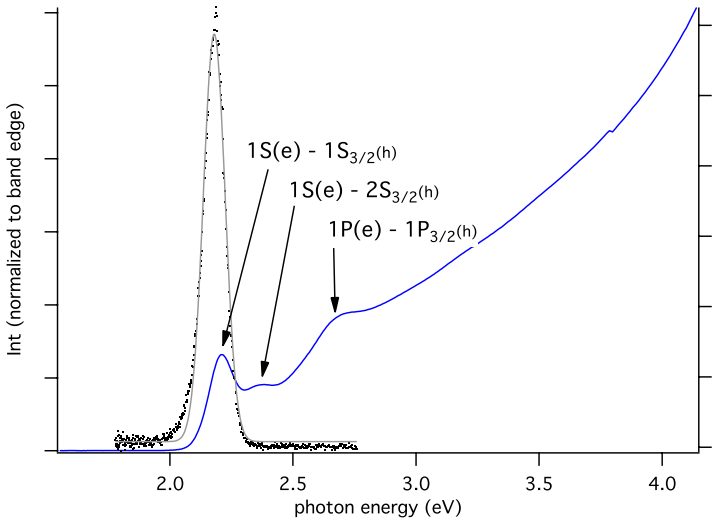

Figure 3. Bulk absorption spectrum for CdSe nanocrystals dissolved in chloroform (blue curve), along with the Stokes shifted emission spectrum (black dots) fitted with a Gaussian function (grey curve). The spectral features are labeled with the electron and hole states involved in the transition.

wavefunction into the capping layer, which can be solved by matching boundary conditions at $r = a$ and ensuring that the wavefunctions vanish appropriately at large r.[17]

1.3 CdSe-OPV Nanostructures for Enhanced Thin Film Packing and Enhanced Photophysics

Blends of colloidal QDs with charge transport polymers are of interest in photovoltaic applications, because electronic coupling between the two moieties has potential for enhanced charge separation properties. However, early attempts at incorporating standard, surface passivated QDs into charge carrier transport layers, such as polyphenylene vinylene (PPV) derivatives and poly (3-hexylthiophene) P3HT blends, resulted in phase segregation between charge transport materials and QDs, leading to poor photoinduced charge mobility at all but the highest (>50% wt/wt) QD loading fractions, where dot-to-dot contact facilitates charge movement.[18]

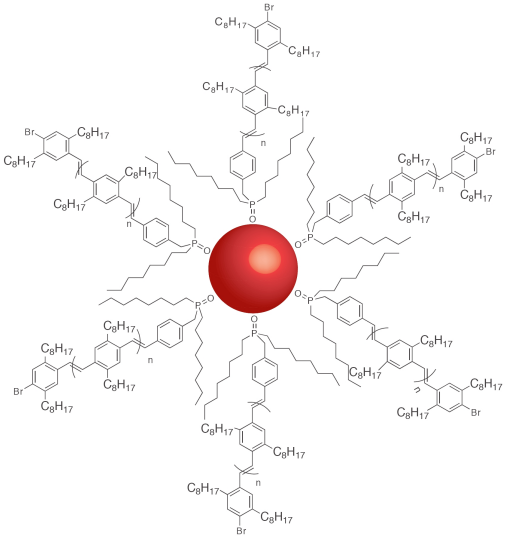

Figure 4. Schematic representation of CdSe-OPV nanostructure.

To overcome this issue, Skaff *et al.*[19] modified the QD surface by exchanging TOPO ligands with di-*n*-octylphospine oxide/phenyl bromide (DOPO-Br) molecules, which were then polymerized to form nanostructures composed of CdSe QDs functionalized with oligomeric PPV chains, referred to as CdSe-OPV (see fig. 4). When deposited in thin films, CdSe-OPV nanostructures demonstrate well-mixed QD/organic phases. Furthermore, solution and solid state photoluminescence measurements showed

interesting results: in solution, CdSe-OPV emission was dominated by the organic ligands, while in the solid state the fluorescence is dominated by QD emission. In contrast, similar measurements on blends of PPV and CdSe nanocrystals showed dominant organic emission in both phases. These measurements suggested enhanced electronic communication between the grafted CdSe-OPV system.

Odoi *et al.*[20] followed on these measurements by examining the photoluminescence properties of single CdSe-OPV nanostructures. These measurements revealed that the photoluminescence from individual CdSe-OPV particles is dominated by the QD core, with intermittent and minor contributions from the organic moiety. Further, single CdSe-OPV hybrid nanostructures displayed enhanced fluorescence properties in comparison to both 'bare' CdSe nanocrystals (QDs covered with DOPO-Br precursor ligands) and CdSe/ZnS core-shell QDs. CdSe-OPV showed considerable resistance to irreversible spectral photodegradation (blue-shifting in emission due to the formation of an oxide layer at the QD surface), as well as reduced fluorescence intermittency ('blinking') under continuous wave illumination. These studies showed strong quenching of oligo-PPV emission via energy transfer to the QD core, resulting in stable emission centered at the QD emission wavelength. This sparked interest in this group for further exploration of CdSe-OPV nanostructures as candidates for enhanced active layers in photovoltaic devices, as well as studies into the fundamental properties of the mechanisms and rates of electronic communication between semiconducting organic moieties and quantum dots.

In what follows, the results of these further studies on CdSe-OPV are described. In Chapter 2 correlations between ligand coverage and reduction in fluorescence

intermittency are explored, where a charge transfer mechanism is proposed to explain these observations. In Chapter 3, the observation of periodic behavior in intensity fluctuations is detailed. Coverage dependence is again observed, but is manifested in the frequency of these fluctuations. Adaptation of Marcus theory-based models aid in explaining this behavior. In Chapter 4, the nature of the electric dipole transition in CdSe-OPV is explored using advanced polarization spectroscopic techniques. Single hybrid nanostructures are shown to display transition dipole moments of both organic and inorganic moieties. Finally, in Chapter 5 experiments are detailed in which evidence for charge separation in the organic moieties drives a Stark shift in QD photoluminescence, which can be controlled by tuning pump polarization. Calculations are described in which a proximal electron at the QD surface perturb the excitonic wavefunctions, providing a natural explanation for both the observed Stark shifts and modified electric dipole transitions in single CdSe-OPV nanostructures.

Information in this thesis is found in a series of publications. Studies on blinking suppression and intensity fluctuations are found in reports by Hammer *et al.,*[21] Early, *et al.,*[22] and Odoi *et al.*[23] Further studies on photon pair correlation experiments to explore multichromophoric behavior in CdSe-OPV are detailed in an article by Odoi *et al.*[24] Information on polarization spectroscopy of single CdSe-OPV nanostructures can be found in papers by Sudeep *et al.*[25] and Early *et al.*[26].

CHAPTER 2

COVERAGE-MEDIATED BLINKING SUPPRESSION IN CdSe-OPV

2.1 Introduction

Fluorescence intermittency, or 'blinking', in single quantum dots has been an area of great interest in single molecule chemical physics since its discovery. It is also a source of frustration from an applications perspective. Processes requiring stable emission from quantum dots, including quantum information processing and *in vivo* tracking of biological labels, suffer greatly from these sudden breaks in radiative recombination, which can occur on a large range of times scales. The statistical properties of single QDs have been studied in great detail as a function of local environment and morphology.[27-32] In contrast, few studies have dealt with the problem of suppressing blinking in individual QDs. Studies in aqueous solution have shown that thiols[33, 34] and propyl gallate[35] molecules are effective in suppressing blinking. Alternative methods, wherein CdSe QDs are overcoated with large[36] or alloyed[37] shells, have been shown to be effective. In what follows, blinking suppression in single CdSe QDs coordinated with OPV ligands is demonstrated. A strong correlation between measured nanostructure diameter (and hence degree of functionalization) and blinking suppression is observed, which points to passivation of surface trap states by the organic ligands as the cause of suppression.

Synthetic breakthroughs by Emrick and coworkers[19, 25] have resulted in the production of QDs coordinated with semiconductor PPV oligomers. These nanostructures, as noted previously, have been shown to exhibit remarkable

photophysical properties; in solution-phase *absorption* measurements, CdSe-OPV nanostructures behave as the constituent parts (i.e. absorption spectra are superpositions of OPV and QD spectra). However, when cast in thin films, *emission* properties are dominated by the QD, suggesting efficient energy transfer from ligands to the QD core.[19] Subsequent studies by Odoi *et al.* confirmed this to be the case for individual CdSe-OPV nanostructures. Excitation in the heart of the OPV absorption spectrum resulted in narrow (~10 nm FWHM) emission peaks centered at the QD emission wavelength.[20] Further studies showed a remarkable degree of stabilization of the QD emission peak in single CdSe-OPV nanostructures. An absence of spectral blue-shifting, which arises from the destruction of the surface layers of the QD and further exciton confinement, was observed in CdSe-OPV. In the same study, a qualitative reduction in blinking events was observed in these spectral measurements.[21] In what follows, we quantify this reduction in blinking and examine the relationship between blinking suppression and particle morphology.

2.2 Blinking in Single Quantum Dots

Blinking in single quantum dots has been known since the first reports by Nirmal *et al*.[38] in 1996. Blinking refers to an abrupt switching from an emissive state to a non-emissive state, which can last from milliseconds to minutes, followed by a return to the radiative recombination cycle. Since those first reports, a large body of literature has been devoted to studying the mechanism and statistics behind this process. [27-32] Many physical models have been proposed to explain this behavior, including three-level systems (ground/excited/trap),[28] tunneling,[29] and Auger ionization models.[39] Blinking intervals have been observed over 9 decades in time.

Figure 5A shows blinking behavior explicitly for a single CdSe/ZnS QD under continuous wave (CW) laser illumination at 405 nm. These plots, displaying fluorescence intensity as a function of time, are referred to as fluorescence trajectories throughout. Blinking events occur on time scales faster than 10 ms (the integration time, and thus lower limit on temporal information, of the experiment). Figure 5B shows a zoom of the fluorescence trajectory in (A) over a period of five seconds, along with a dotted line signifying the on-off threshold value. The two sections denoted τ_{on} and τ_{off} refer to two individual on- and off-intervals. On this data scale, fluorescence transitions ranging from10 ms up to 500 ms can be observed.

Histograms of τ_{off} and τ_{on} for 18 QDs are shown in figs. 5C and 5D, respectively, in log-log plots. The plots are fit with power law fits of the form $P(\tau) = \tau^{\alpha}$, with exponents α_{off} = -1.43 and α_{on} = -1.24, in good agreement with observations of α ranging from -1 to -2, with most groups reporting $\alpha \approx$ -1.5.[29, 40-43] The form of these distributions rules out mechanisms involving static trapping states, as these models lead to exponentially distributed trapping kinetics in all cases. As will be discussed further in Chapter 3, we find that models based on distributed, fluctuating trapping states, which yield power law blinking kinetics, account for many behaviors observed in CdSe-OPV. In Chapter 3, several other models are outline which attempt to explain power law behavior for both on- and off-time distributions. Such blinking events, while of fundamental interest from a chemical physics perspective, are highly problematic in device applications, and attempts to eliminate blinking based on a number of different methods have been detailed.

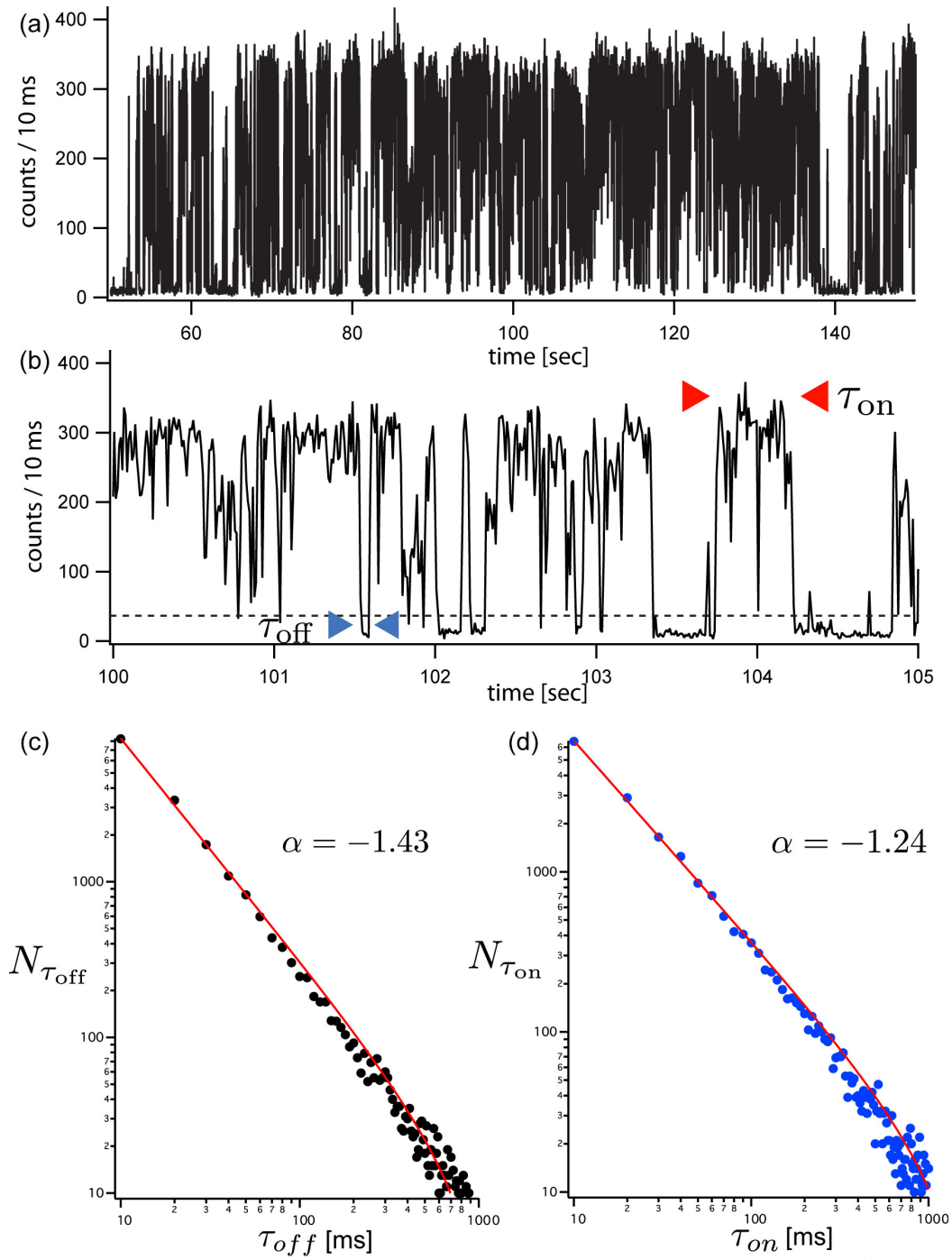

Figure 5. (a) Fluorescence behavior under continuous wave illumination for a single CdSe/ZnS nanocrystal. Photon counts are binned in 10 ms intervals. Blinking events occur on time scales from <10 ms to tens of seconds. (b) Zoom of the trajectory in (a) from 100-105 sec, explicitly showing t_{on} (red arrows) and t_{off} (blue arrows) intervals. (c) Compiled histogram of off-intervals for 18 QDs plotted on a log-log scale, yielding a power law exponent of α = -1.43. (d) Histogram of on-intervals for the same particles, with α = -1.24.

2.3 Experimental

To obtain both topographical and fluorescence data from single CdSe-OPV nanostructures, we employed an inverted fluorescence microscope modified with a top-mounted atomic force microscope (AFM). Figure 6 shows a schematic experimental diagram. Individual CdSe-OPV nanostructures were isolated from dilute tetrahydrofuran solution (~10^{-10} M) on clean glass coverslips. We used 457-nm radiation from a continuous wave Ar+ laser (≈ 200 μW power; 15 μm diameter spot size) as the excitation source. All fluorescence imaging and spectroscopic measurements were obtained under ambient conditions using a Nikon TE300 inverted microscope with a 1.4 NA oil objective in a total internal reflection (TIR) configuration. AFM measurements were performed in Tapping Mode using a Digital Instruments Bioscope model BS3-N mounted directly to the microscope. Fluorescence images were acquired with a Princeton Instruments PhotonMax CCD camera, with exposure times of 100 ms to 2 s and a typical total observation time of 1000 s. Initial registration of fluorescence and AFM surface height images was performed using 20-nm FluoSpheres (Invitrogen Corporation).

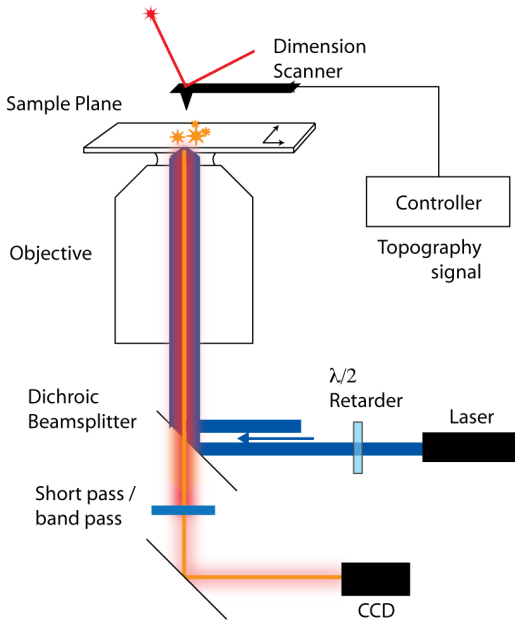

Figure 6. Experimental setup for correlated AFM/fluorescence measurements. See text for details.

In a typical experiment, a sample is cast onto a coverslip and imaged in fluorescence mode to obtain spatially distinct single molecules. After brightfield

alignment of the AFM cantilever with the objective focus, the AFM scanner is disengaged and fluorescence data is collected. When complete, the pump laser is blocked and the AFM head is engaged to scan the area, yielding both topographical and fluorescence data from individual nanostructures which we spatially correlate offline using image processing software (Igor Pro, Wavemetrics). We find negligible structural changes in CdSe-OPV nanostructures before and after laser illumination.

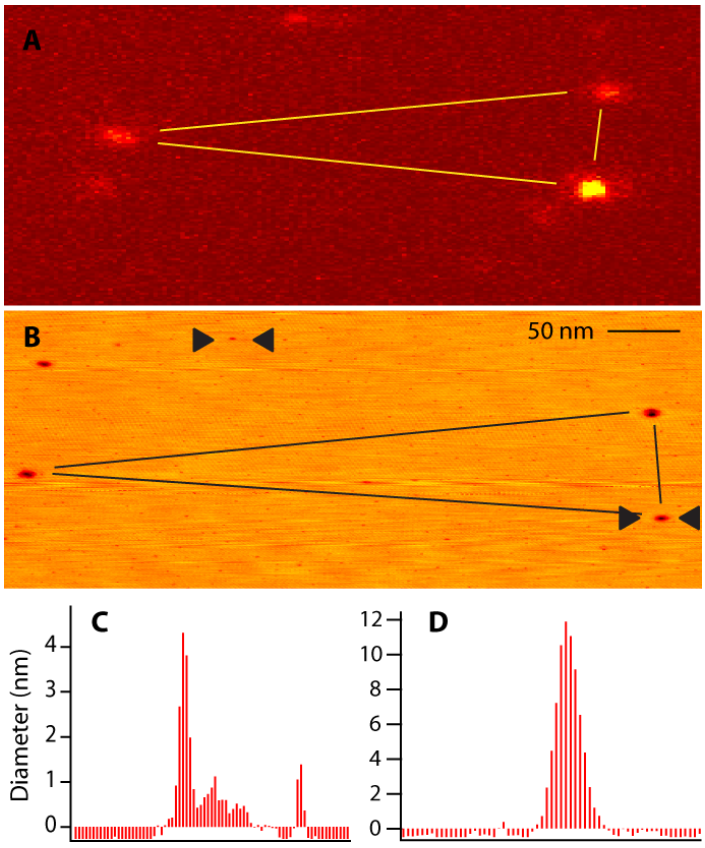

Figure 7. Correlated fluorescence (a) and AFM (b) images for individual CdSe-OPV nanostructures. The guidelines are to highlight deposition patterns. Scale bars are labeled in (b). (c) AFM line profile for the upper structure, and (d) line profile for the lower structure.

Figure 7 shows a typical AFM/fluorescence micrograph for single CdSe OPV nanostructures, with single-frame fluorescence information (a) and AFM topographical in (b). Typically, fluorescence data was collected for 1000 s to gather well-converged statistics. Figure 7(c) and (d) show AFM line profiles from the particles bracketed by the upper and lower sets of arrows in the AFM image in (b). For the lines scans the relevant dimension is the height dimension, as the lateral signatures are a convolution of the AFM tip shape (approximated as a half-

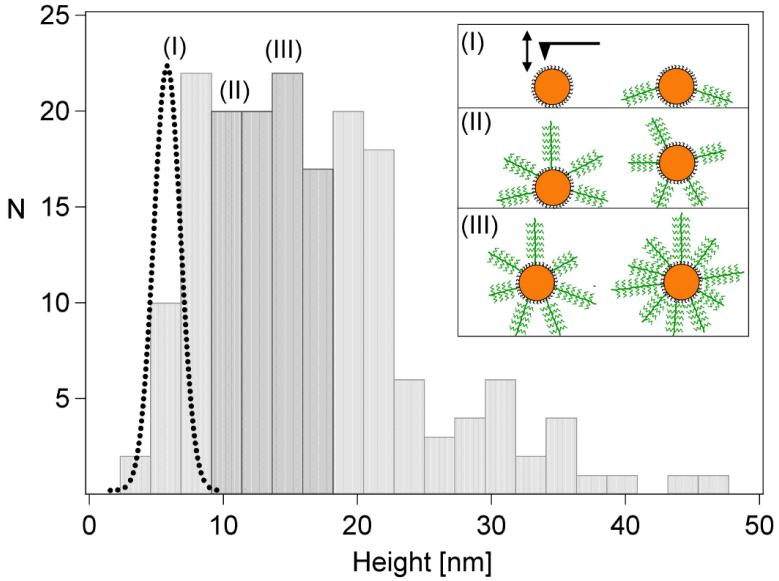

Figure 8. Histogram of particle heights for 180 CdSe-OPV nanostructures determined by AFM. The dotted line shows the AFM height distribution of the CdSe precursor. Inset: Three different coverage regimes are depicted: (I) bare, (2) partial, and (3) fully coordinated nanostructures.

sphere with radius of curvature ~ 20 nm) and the particle lateral dimensions. As shown in (c) and (d), considerable heterogeneity in particle diameter exists using the *in situ* polymerization (the so-called "graft-from" synthesis method) of polymer chains from the QD surface. The particle in (c) exhibits a height signature of a 'bare' (CdSe-TOPO) nanocrystal, whereas the larger structure in (d) represents a fully covered structure (4 nm core + 2(4 nm OPV)).

A histogram of particle heights for 180 CdSe-OPV nanostructures is shown in Figure 8. The dashed line centered at ~6 nm represents the distribution of heights of the CdSe-OPV precursor (CdSe-DOPO-Br). After the 'graft-from' polymerization of the precursor, the resulting particles show a large degree of heterogeneity in surface coverage. In fig. 8, three different size regimes are indicated in the inset and on the histogram: (1) 'bare' nanocrystals, (II) partially coordinated, and (III) completely

coordinated, which are depicted schematically in the inset. Because of this heterogeneity in ligand length and coordination environment, the ability to size select and analyze photophysical properties from subsets of nanostructures based on coverage extent is crucial to understanding structural effects on emission behavior.

2.4 Size-dependent Emission Statistics

Using the techniques detailed above, we collected emission statistics for hundreds of individual CdSe-OPV nanostructures, each tagged with a particle diameter. We see a strong reduction in fluorescence intermittency in CdSe-OPV particles in comparison to both CdSe/ZnS core-shell QDs and the CdSe-DOPO-Br precursor. Figure 9 shows intensity trajectories for both a CdSe/ZnS QD (left) and a CdSe-OPV nanostructure (right) using 1 second integration times, along with the on/off threshold for both. In these trajectories, the threshold is determined by examining nearby background CCD pixels and calculating the 2σ value. This value is then added to the background-subtracted data,

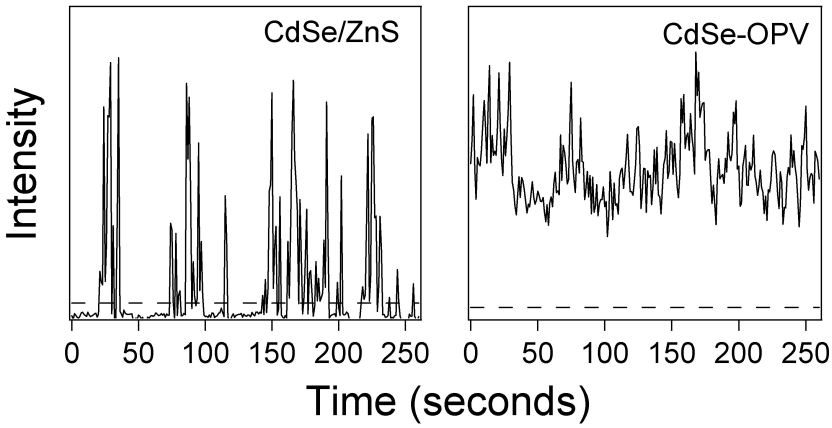

Figure 9. Intensity trajectories for a CdSe/ZnS QD (left) and a CdSe-OPV nanostructure (right) under identical excitation and collection conditions using a 1 sec integration. The on/off threshold is shown with a dotted line in each.

with any values above this threshold considered "on" and those below "off." From these data, clear and complete blinking suppression is seen in CdSe-OPV, with significant on-state fluctuations present. In comparison, CdSe/ZnS shows short fluorescence bursts, as described previously. In the experiments on CdSe-OPV, band pass filters were used to ensure only QD fluorescence (no ligand contribution) is collected. Therefore, vestigial fluorescence from the coordinated ligands cannot account for the observed blinking suppression.

Because CdSe-OPV nanostructures in general show highly reduced blinking (i.e. on-to-off and off-to-on transitions), the blinking analysis described above breaks down. To quantify this phenomenon, we instead calculate the total fraction of experiment time a particle spends in the emissive state (referred to as fluorescence duty factor or FDF), using the same threshold criteria described above. Figure 10 shows histograms of FDFs for CdSe/ZnS QDs and CdSe-OPV nanostructures. In (a), the distribution of FDFs for

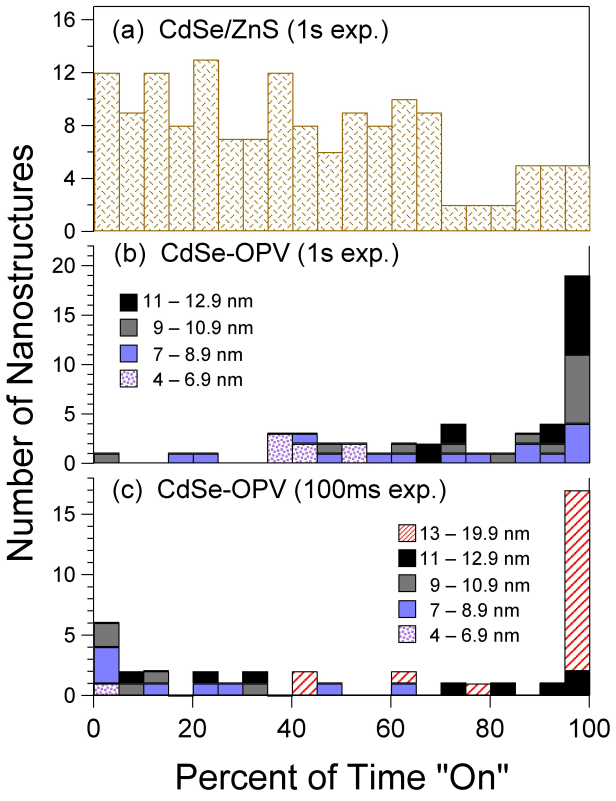

Figure 10. Distribution of fluorescence duty factors for (a) CdSe/ZnS QDs, (b) CdSe-OPV nanostructures at 1 sec integration time, and (c) CdSe-OPV nanostructures at 100 ms integration time. In (b) and (c), histograms are color-coded by measured particle size.

CdSe/ZnS varies from 1%-95%, with a mean value of 40%. In Fig. 10(b), FDFs for CdSe-OPV nanostructures under 1 second integration times are shown. In the smallest size range (4-7 nm), FDFs are essentially indistinguishable from bare QDs, while the average FDF jumps to ~70% for particles in the 7-10 nm size range. At the largest particle sizes (11-13 nm), particles spend virtually 100% of the experimental observation time in an emissive state. When the integration time is dropped to 100 ms in Fig. 10(c), blinking becomes observable. Nanostructures in the fully-covered regime (11-13 nm) exhibit average off times $\langle \tau_{off} \rangle \approx 500\text{ms}$. These histograms clearly highlight the importance of ligand coverage in suppressing blinking behavior.

Although on-off transitions in single CdSe-OPV particles are not commonly observed using 1 second integrations, the fluorescence intensity does not exhibit steady state behavior (see Fig. 9, for example). This is most easily seen in histograms of fluorescence intensities for the

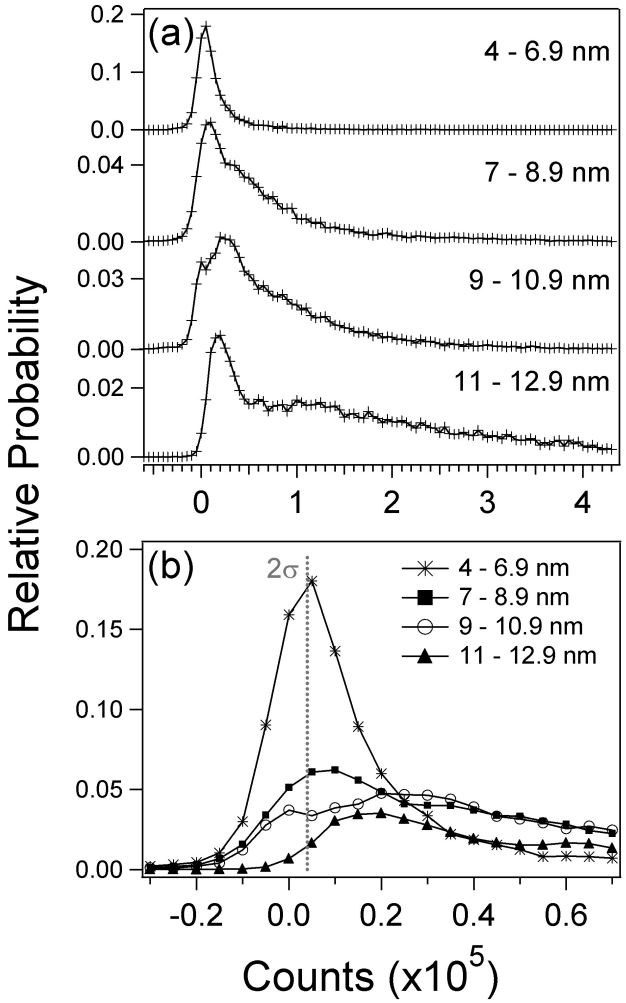

Figure 11. (a) Normalized intensity histograms of the particles in fig. 10B, according to particle height. (b) Zoom of the intensity region near the 2σ on-off threshold.

size regimes described above in Fig. 11. In Fig. 11(a) are normalized histograms of emission intensities for the different size classes. Bare particles exhibit average intensities of 2.1×10^4 counts, which jump to 1.7×10^5 counts for fully covered particles. Fig. 11(b) shows a zoom of the count region near the 2σ threshold level; all probability density above this line represents the FDF for each particle class.

While the bare QDs exhibit largely symmetric intensity distributions, the larger particles take on much more structure out toward higher count rates. This suggests the presence of a dynamic process underlying the blinking suppression observed here. We propose a mechanism based on the passivation of trap sites at the QD surface, which trap charge carriers and prevent radiative recombination when occupied. This passivation is accomplished by photoexcitation of the coordinated organic ligands, which in turn act as electron donors, transferring charge to available surface traps. In this picture surface trap passivation should scale linearly with particle coverage, which we see evidence for in the size-correlated measurements. In Chapter 3 and 5 this mechanism will be studied in moredetail, and we find further evidence supporting this hypothesis.

CHAPTER 3

INTENSITY RECURRENCES IN SINGLE CdSe-OPV NANOSTRUCTURES

3.1 Introduction

Semiconductor quantum dots (QDs) are well known for their size-tunable optical and electronic properties, broad optical absorption spectra, and narrow emission spectra that make them attractive in applications such as biological labeling,[44, 45] photovoltaic devices[6], and single photon emitters.[46] However, the issue of fluorescence intermittency (blinking) is problematic in many of these applications, and has been the subject of many recent experimental and theoretical studies. A number of interesting features of QD photoluminescence have been well documented including inverse power law blinking kinetics,[29, 47] statistical aging in intensity autocorrelation measurements,[48, 49] radiative rate fluctuations,[50] and spectral diffusion.[31, 51] Recently, we and others reported suppression of QD blinking behaviour, either as a result of coordination of the QD surface with suitable organic ligands[21, 34, 50] or other environmental parameters.[52, 53] The qualitative picture proposed for blinking suppression in these systems involves carrier trapping at the QD surface from electron-donating moieties, which in turn enhances the relative probability of radiative recombination within the QD.

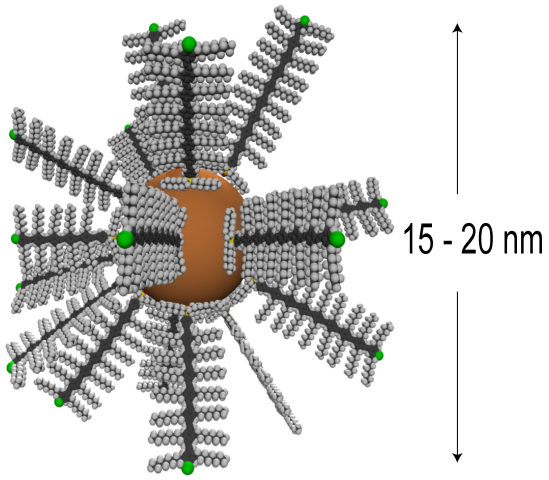

Figure 12. Schematic illustration of a CdSe-OPV composite nanostructure, as determined from size-correlated fluorescence measurements [20]. The QD diameter is 4.5 with ~10% monodispersity. Composite particles range in size from 10 -25 nm, depending on ligand coverage

We recently reported on the photoluminescence dynamics of CdSe

quantum dots functionalized with para-phenylene vinylene oligomers (CdSe-OPV) [19]. These composite nanostructures (schematic illustration included as figure 12) exhibited enhanced spectral stability and significantly reduced blinking, with average dark-state dwell times on the order of 500 ms, compared to tens of seconds for ZnS-capped quantum dots [20]. Time-resolved spectral studies of individual CdSe-OPV nanostructures showed that virtually all of the photoluminescence is associated with the QD, indicating that excitations within the organic ligands are efficiently quenched by energy transfer and/or charge-transfer processes facilitated by the molecular architecture [21]. Here, we discuss the experimental observation and kinetic modeling of QD "*flickering*," where the fluorescence intensity trajectories show a broad distribution of bright states, and reveal the existence of recurrence features apparent in the fluorescence intensity trajectories of individual CdSe-OPV composite nanostructures. Finally, we present results of numerical simulation of photoluminescence intensity trajectories based on an extension of the diffusive coordinate (DC) model proposed recently by Frantsuzov and Marcus [40]. We show that such a model will yield a pseudo-periodic behaviour in the fluorescence intensity as a result of fluctuations of the coordinate *e* (the energy separation between S and P excitonic states).

3.2 Size-dependent Fourier Analysis of Intensity Trajectories

CdSe-OPV nanostructures were prepared by polymerization of aromatic vinyl bromides from the surface of functionalized quantum dots [19], resulting in a distribution of nanostructure sizes [21]. All dilutions were made in high purity tetrahydrofuran (THF) to single molecule concentration (~100 pM) and deposited on plasma-cleaned glass coverslips (< 1 quantum dot/μm^2). Fluorescence imaging was performed under ambient

conditions on an inverted microscope (Nikon TE300) in total internal reflection geometry through a 1.4 NA oil objective. Emitted light was collected through the same objective, filtered using a dichroic beamsplitter and filter set and sent to an EMCCD array (Princeton Instruments/Acton PhotonMax). Height signatures for individual CdSe-OPV nanostructures were obtained by AFM in TappingMode (Digital Instruments Bioscope) and correlated with fluorescence images as described previously [21].

Figure 13 shows intensity traces and corresponding power spectra for three representative nanostructures of diameter (a,d) 16.0 nm, (b,e) 21.9 nm, and (c,f) 23.9 nm. As discussed previously, the CdSe-OPV nanoparticle size distribution derives from various degrees of surface coverage. As illustrated, the fluorescence trajectories of these particles exhibit well-defined recurrence times on scales of 10 - 50 seconds, which are reflected in the power spectrum for each particle. No such recurrences were observed from control trials using 20 nm dye-doped polystyrene nanospheres (Invitrogen, Molecular Probes Fluospheres) indicating that the recurrences are not associated with camera artefacts or laser intensity fluctuations.

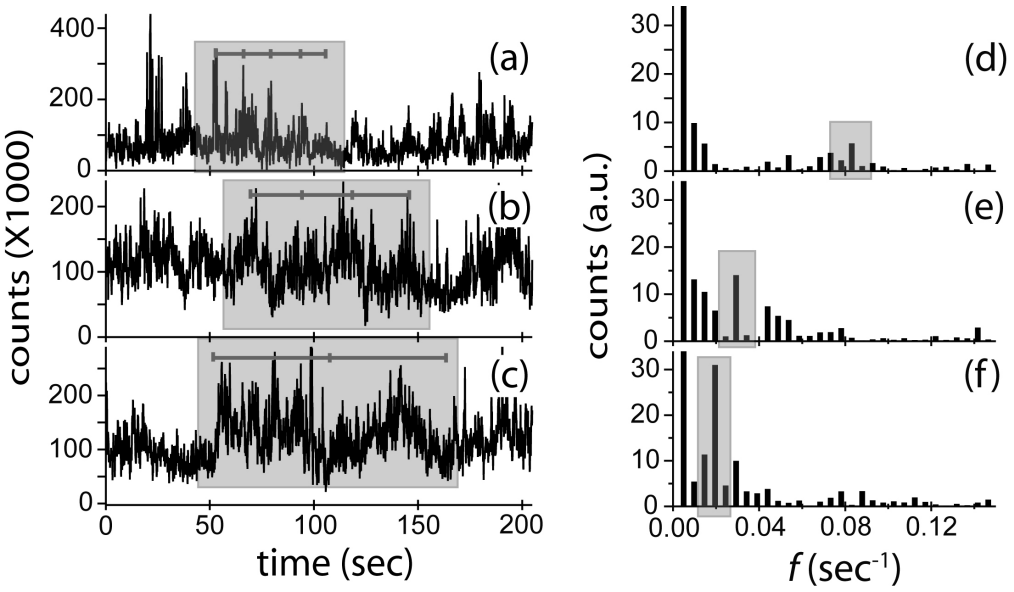

Figure 13. Representative photoluminescence intensity trajectories and corresponding power spectra for three CdSe-OPV nanostructures of diameter (a,b) 16.0, (c,d) 21.9, and (e,f) 23.9 nm. Recurrence features are highlighted in intensity trajectories along with corresponding spectral components.

Figure 13 also shows the growth in low frequency spectral components with increasing nanostructure diameter that were present in some degree for every nanostructure imaged. Evidence of the characteristic frequency scaling with ligand coverage will be discussed elsewhere. For sparsely functionalized nanostructures (evidenced by surface height signatures comparable to bare QDs), such as that represented in figure 13(d), the fluorescence flickering is characterized largely by low amplitude, high frequency noise. As surface coverage increases (figure 13(f)), large amplitude, low frequency peaks (longer recurrence times) become evident in the power spectrum. This trend indicates an oscillating relaxation rate which is highly sensitive to the presence of OPV ligands coordinated to the QD surface.

3.3 Models for Quantum Dot Blinking

As described previously, models for quantum dot blinking have been proposed since the first experimental observations by Nirmal *et al.*[38] Some of the earliest models were based on schemes lifted from so-called 'quantum jump' models for atomic fluorescence.[54, 55] These reports on 'random telegraph' fluorescence from single quantum dots[28] were based on a long-lived charge separated model, where radiative exciton recombination is interrupted by QD ionization and ejection of a charge into the surrounding matrix. The states involved the random telegraph model are shown in figure 14, where $|0\rangle$, $|1\rangle$, and $|2\rangle$ are the number of excitons in each state, $|+\rangle$ is the ionized state, $W_{1,2}$ are the pumping rates, $k_{1,2}$ are the relaxation rates from states 2 and 1 (k_1 is the radiative rate), and k_A and k are the Auger ionization rates and rate of detrapping from the dark state, respectively.

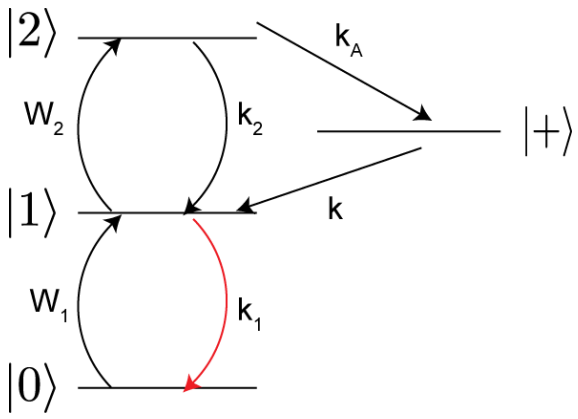

Figure 14. States and transitions involved in the random telegraph blinking model. The numbered states refer to the number of photogenerated excitons (+ is the ionized state), W_i are the interstate pumping rates, and k_i are the interstate relaxation rates. The radiative transition k_1 is shown in red.

In this model, ionization can occurs via Auger autoionization and the QD is rendered 'dark' until thermal return of the charge to the QD. This model, while qualitatively recovering the on-off blinking transitions, *cannot recover* some fundamental experimental observations. Namely, the existence of inverse power law distributions of on- and off-times cannot be described by this model, because the return rate from the dark shelved state to an emitting state is governed by a single rate constant. This will

always yield *exponential* on/off time distributions when solving for steady-state populations. For this reason, several models have been proposed to overcome this inconsistency with experimental observations.

Attempts have been made to correct the problems with the random telegraph model described above by assuming an exponential distribution of trapping states of the form $\rho(E_{trap}) \propto \exp(-\alpha E_{trap})$. Escape of ejected electrons from these trap states is then dictated by an Arrhenius mechanism with a rate $k = A\exp(-\beta E_{trap})$. While models of this form correctly predict the form of $P(\tau_{off})$, they don't recover the trapping the probability of on-time distributions $P(\tau_{on})$, because all forward rates for trapping get combined into one forward rate, which again predicts an exponential on-time distribution at odds with experimental results (see fig. 5). Such a model would also predict temperature dependence on the on- and off-time, which has not been observed for single QDs even down to liquid He temperatures.

For these reasons, new models for blinking have evolved to take into account all of the factors described above. Application of Marcus theory to quantum dot kinetics was recently proposed in papers by Frantsuzov[40] and Tang[56, 57] in so-called diffusion-controlled electron tranfer (DCET). In these formulations, both spectral diffusion and blinking stem from light-induced diffusion of QD energy levels. The nature of the light-induced diffusion is thought to occur via small lattice rearrangements on absorption and emission of photons, although the physical mechanism of this rearrangement is not well-defined in theses reports. This model correctly predicts long-time behavior and dependence on temperature and pumping intensity for $P(\tau_{on})$ and $P(\tau_{off})$. A collaborative theoretical and experimental investigation by Pelton *et al.*[58] verified some predictions of

DCET theory by correlation analysis of single photon arrivals. Because of the success of this model in predicting photophysical behavior of CdSe/ZnS core-shell QDs, we adapted aspects of this model for explanation of the observed intensity fluctuations in individual CdSe-OPV nanostructures. Namely, the inclusion of a fluctuating hole-trapping rate that depends on the QD *1S* and *1P* electron spacing recovers the observed intensity fluctuations. This also makes an appealing physical picture, where the spatially extended *1P* wavefunctions are heavily influenced by the presence of ligands.

3.4 Diffusive Coordinate Model

Many models have been proposed to explain blinking rates in quantum dot systems, ranging from photoinduced charging models[28] to multiply charged surface site models.[59] However, the DC model proposed by Frantsuzov and Marcus[40] is attractive for describing CdSe-OPV emission behaviour due to its incorporation of a diffusive non-radiative coordinate in a harmonic potential. Coupling of this diffusive motion to non-radiative decay rates will naturally lead to bounded, slowly evolving trajectories in the photoluminescence intensity, as observed in our experimental data. Here, we show that an extension of this model, with some changes assumed in the form for non-radiative relaxation due to Auger-assisted hole trapping, yields the observed trend in recurrence time scale through variation of two parameters that may be related to the presence of complex ligands such as OPV. In the DC model, light-induced diffusional fluctuations in the quantum dot "environment" (that is, all degrees of freedom aside from the two-level system describing ground and excited states) have a strong influence on hole-trapping processes that act as non-radiative relaxation processes.

In this picture, the parameter $\varepsilon = E_{1Pe} - E_{1Se}$ (the difference in energies between

the lowest two above-gap electronic states) takes on the role of a slowly diffusing reaction coordinate that describes (by proxy) structural or electronic changes at the surface of the quantum dot. Such changes are assumed to be dominated by light-induced conformational changes occurring at the surface during absorption and radiative relaxation processes. By way of conservation of energy, ε (in conjunction with the lineshape of the surface states) dictates directly the rate of Auger-assisted trapping of the excitonic hole in an intra-gap band of surface states, leading to efficient non-radiative relaxation of the exciton and subsequent modulation of the photoluminescence intensity.

Figure 15(a) illustrates the processes that dictate photoluminescence intensity in the DC model, as well as the role of ε in modulating the hole trapping process, as originally described by Frantsuzov and Marcus.[40] Auger-assisted hole trapping is assumed to split the dynamics into a non-radiative path (light blue arrows) that competes

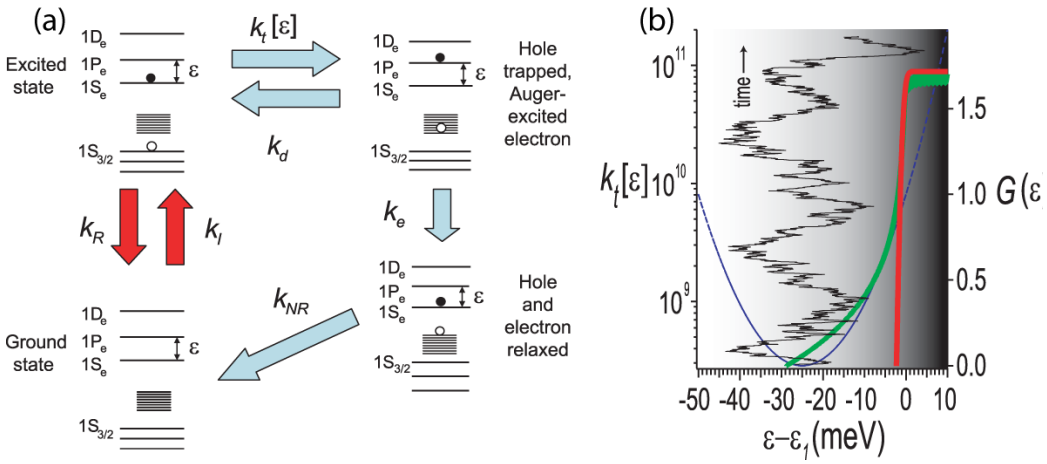

Figure 15. (a) QD states and kinetics relevant to the photoluminescence of CdSe-based nanostructures, following the DC model of Frantsuzov and Marcus. The photon absorption rate k_I and radiative relaxation rate k_R compete with the non-radiative path (light blue arrows) resulting in strong fluctuations in photoluminescence intensity. The rate for hole de-trapping is assumed to be similar to k_t [ε]. k_e is the rate for phonon-assisted $1P_e$ to $1S_e$ transition. k_{NR} is the rate for final non-radiative recombination of the electron-hole pair. (b) The parabolic potential (dotted blue trace, right axis) controlling diffusion of ε, superimposed on the Gaussian or strong-coupling (solid red trace, left axis) form and the Lorentzian or Breit-Wigner (solid green trace, left axis) form of the Auger-assisted hole-trapping rate. Regions of ε corresponding to large values of k_t[ε] are associated with dark states. A simulation of biased walk in ε is overlaid (bottom axis).

kinetically with the radiative path (red arrows). It is via the ε -dependence of the Auger hole-trapping rate that diffusive dynamics of the environment (surface, etc.) influence the importance of the non-radiative path. Where possible, experimentally-determined values for rates and energy values have been used (see Appendix C). In figure 15(b), we have plotted the parabolic diffusion potential alongside the trapping rates for the two cases. We find that a Breit-Wigner or similarly slowly varying form of the hole-trap lineshape function is essential for recovering the experimentally observed intensity fluctuations. The grey-scale background is designed to indicate relative luminescence brightness correlated with the random variable (ε - ε_0). From this picture one can see how the sharp cut-off of the Gaussian form leads to high-contrast "on-off" behaviour, while the more slowly varying Breit-Wigner form leads to a "flickering" behaviour, represented as a continuum of grey levels.

Tang and Marcus[60] have used similar arguments to explain the ubiquitous phenomena of spectral diffusion in semiconductor quantum dots with some encouraging agreement with experiment.[61] In this case, it is the excitation energy E_{ex} itself that undergoes diffusion, resulting in a drift of the emitted photon energy on time scales of seconds. The quasi-binary behaviour fluorescence intermittency via diffusion of ε, was shown to be closely associated with the functional form of the Auger-assisted hole-trapping rate on *e* that Frantsuzov and Marcus defined as[40]

$$k_t[\varepsilon] = \alpha \sum_i \exp\left[-\frac{(\varepsilon - \varepsilon_i)^2}{\beta^2}\right]$$

where the index *i* runs over the ~ 200 trap states postulated to be formed by Se dangling bonds on the surface of the dot. Based on some reasonable parameters, the conclusion was that the diffusion of ε occurs over large amplitudes that brings ε into and out of the

region of very large trapping rates. Visitations into these regions associated with large values of $k_t[\varepsilon]$ result in long dark periods, while excursions out of the region of large trapping rate yield the bright regions within the trajectory.

In order to explain the blinking suppression and the presence of long-time recurrence features in photoluminescence intensity, we must have either diffusion of ε limited to amplitudes over which the Auger-assisted trapping rate is always in competition with the rate for radiative recombination, or a different, long-tailed form for the hole-trapping rates than assumed in the previous model. We take the latter approach and find that the assumption of Breit-Wigner (Lorentzian) lineshapes and trapping rate

$$k_t^{BW}[\varepsilon] = \alpha \sum_i \frac{\left(\frac{\beta}{2}\right)^2}{\left(\frac{\beta}{2}\right)^2 + \left(\varepsilon - \varepsilon_i\right)}$$

as opposed to the strong-coupling or Gaussian form assumed above, gives the necessary photoluminescence dynamics needed for extending the ideas of DC theory to CdSe-OPV nanostructures. We also assume a reduction in ε_0, the bare value of the energy difference E_{1Pe}-E_{1Se}. These "ansatz" alterations of the DC model for CdSe-OPV are entirely reasonable in light of the profound effect of the precise nature of the dative phosphine oxide bond to Cd on the dot electronic structure.[62] In general, OPV ligands present a complex electronic and photonic environment of the surface states; such an environment might alter the many-body transition matrix elements in such a way as to yield the necessarily broad form of the hole trapping rate needed for diffusive processes to leave their fingerprint.[63]

3.5 Monte Carlo Simulations

The central idea behind our numerical simulation of fluorescence intensity trajectories is that the number of detected photons within a specific time window is inversely proportional to the overall decay rate expressed as a sum of radiative and non-radiative rates, k_R and k_{NR}. The nonradiative rate constant that competes with k_R is directly related to the instantaneous value of ε, so propagation of a diffusional trajectory in the coordinate ε yields a model of the intensity trajectory. At each step, the steady state solution of the kinetic model of photoluminescence[40] is utilized to calculate the steady state value of the photoluminescence, given ε as the input to the Auger-assisted trapping rate. All data presented assumes constant rates for photo-absorption (absorbed flux of 5.0×10^6), radiative lifetime (20 ns), rate for non-radiative recombination of trapped hole and electron ($\sim 10^6\ s^{-1}$), and a fast, overall rate of the (hole-trapping/electron $1P_e$ to $1S_e$) process ($3 \times 10^{11}\ s^{-1}$). Also constant are the parameters characterizing Breit-Wigner trap state lineshapes ($a = 5.0 \times 10^{10}\ s^{-1}$, $b = 1.0$ meV).

Figure 16 shows simulation results from parameters that yield reasonable agreement with our experimental intensity trajectory data. While the parameter space available to explore in the simulation is very large, we have strived to make the parameters agree as well as possible with estimates in ref. 40. The most notable deviation from the parameters in the original theory is a decreased diffusion amplitude D_e (10-30 meV compared to ~ 90 meV in that paper). However, we stress that the most important

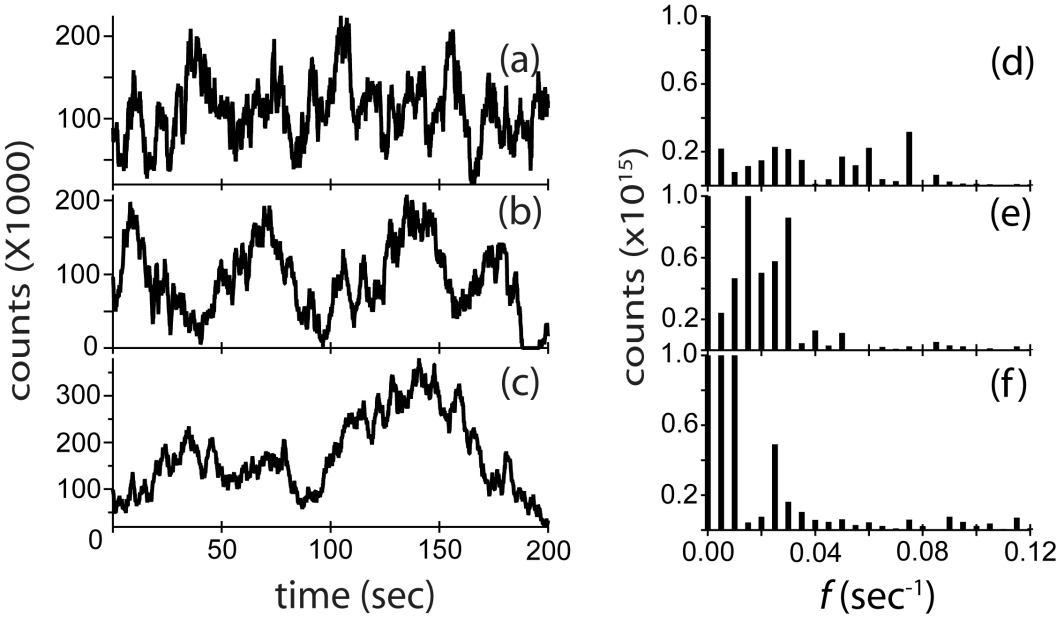

Figure 16. Simulation results for Frantsuzov-Marcus theory using Breit-Wigner form for Auger-assisted trapping rate. From top to bottom: De/ae = 10 meV/2.0 meV, 25 meV/1.6 meV, 30 meV/1.5 meV. Shown also are corresponding power spectra highlighting the specific recurrence features.

factor for agreement with our experimental results is the assumed Breit-Wigner form for the Auger-assisted hole-trapping rate. Figure 16 shows that a simultaneous increase of D_e and lowering of a_e (the size of the light-induced diffusive steps in ε), is a potential mechanism for the increased prominence of low frequency features in the photoluminescence time traces. Since this trend is associated with increased ligand

coverage in our correlated AFM/fluorescence data, we speculate that the effects of the ligand environment on dot energetics may be involved in such a picture.[64]

We find that observed periodic recurrences in the photoluminescence emission intensity from CdSe-OPV nanostructures, and blinking suppression, can be explained using a diffusive coordinate (DC) model similar to Frantsuzov and Marcus with a modified hole-trap lineshape function. We demonstrate via numerical simulation that a modified diffusive coordinate model can reproduce the periodicity and associated amplitude given a large dynamic range (over values of ε) for Auger-assisted hole-trapping. The result of this modification is a more slowly varying k_{NR} which reduces – but does not extinguish – the fluorescence intensity. It is apparent that the important contributions to correctly simulate the photoluminescence dynamics in our CdSe-OPV data are the broader resonances of surface-hole trap states, resulting in a wide region of slowly varying Auger-assisted hole trapping, and constrained excursions of ε to values where blinking to the "off" state can not be observed. The second of these contributions has two possible origins: a reduction in e_0, the nominal value of the $1P_e - 1S_e$ energy difference, or the constrained diffusion of ε to smaller values, or some combination of these two effects. At this point, it is difficult to pinpoint the precise role of the conjugated organic ligands in the modification of the hole-trap lineshape, but the mere presence of the observed recurrences strongly suggests a dynamically varying non-radiative transition rate.

CHAPTER 4

LINEAR TRANSITION DIPOLES IN SINGLE CdSe-OPV NANOSTRUCTURES

4.1 Introduction

We recently reported enhanced spectral stability and suppressed fluorescence intermittency (blinking) in CdSe nanocrystals coordinated with paraphenylene vinylene oligomers (CdSe-OPV).[21] In these nanostructures the OPV ligands serve as a surface passivating layer on the quantum dots, and are spectrally positioned as energy donors in Forster excitation transfer to the nanocrystal acceptor. We speculated that the presence of the capping ligands, in which excitons are generated under continuous wave (cw) illumination, transfer charge carriers to the nanocrystal surface and passivate localized trap sites, thereby also reducing residence times in so-called 'dark states' in photoluminescence. In this scheme, one would expect the polarization characteristics of the organic ligands to be superimposed on the QD in absorption. Here we show that, when excited in a wavelength region where both OPV and CdSe absorb, individual CdSe-OPV nanostructures display both strong linear dichroism *and* linearly polarized emission (manifested in dipole emission pattern imaging), in addition to the previously reported blinking suppression. By tuning the excitation closer to the CdSe band edge and away from the OPV absorption band, these effects are strongly suppressed. We propose a mechanism based on a directional Stark interaction caused by photoproduced excitons in the organic ligands that break the symmetry of the nanocrystal core. These results provide strong evidence of transfer of the linearly polarized transitions

of OPV molecules to pseudo-spherical CdSe QDs, resulting in hybrid structures that display the polarization properties of conjugated organic molecules and the robust photoluminescence of nanocrystalline quantum dots.Numerous theoretical[10, 65] and experimental[12, 51] studies on colloidal QDs have examined the character of the transition dipole moment in CdSe nanocrystals capped with passive surface ligands and/or a ZnS shell. The splitting of the band edge $1S_e$-$1S_{3/2}$ exciton in CdSe nanocrystals into a five-state manifold has been predicted by perturbation theory and verified experimentally[12, 66] (see Fig. 17, left). The so-called "bright exciton" $|1^L>$ state with angular momentum $F = \pm 1$ has been the focus of several recent experiments, in which the structure of the so-called 2D degenerate dipole moment of wurtzite nanocrystals has been verified. This circularly symmetric dipole moment can be represented as an equatorial disk about the minor axis of slightly prolate nanocrystals in the plane perpendicular to the crystalline c-axis. This transition dipole moment structure has been confirmed both by polarization anisotropy measurements[67, 68] as well as imaging of the defocused photon distribution patterns of single crystals[69, 70], which appear as the summed intensity of two orthogonal, independent emitters. These experiments have been used to rapidly determine the lab-frame orientation of the crystal c-axis of individual nanocrystals.

Recent low-temperature experiments by Klimov and coworkers[14] have uncovered a slight degeneracy breaking in asymmetric CdSe/ZnS nanocrystals. In these experiments, the $|1^L>$ state is further resolved into linearly polarized, orthogonal sublevels

$$|X\rangle = \left(1/\sqrt{2}\right)\left(|+1\rangle + |-1\rangle\right)$$

and

$$|Y\rangle = \left(1/\sqrt{2}\right)\left(|+1\rangle - |-1\rangle\right).$$

These sublevels split the 2D degenerate dipole into mutually orthogonal components, resulting from small differences in the exciton exchange interaction at the elliptical equator,[12, 14, 70] shown schematically in Figure 17, right. These components were shown in approximately 10% of the nanocrystals sampled to have a non-zero energy splitting on the order of 1-2 meV, scaling with nanocrystal volume.

Until now, direct visualization of any splitting of this equatorial transition moment has been in the form of modified 2D transition dipoles[71, 72] (i.e. 3 1D dipoles, 2D + 1D dipoles). Such modified transition moments likely arise from sample-to-sample heterogeneities, because the ratio of oscillator strengths between the $|1^L\rangle$ (degenerate) and $|0^{U,L}\rangle$ (linear) transitions depends strongly on crystal shape.[12, 65] In this report, we

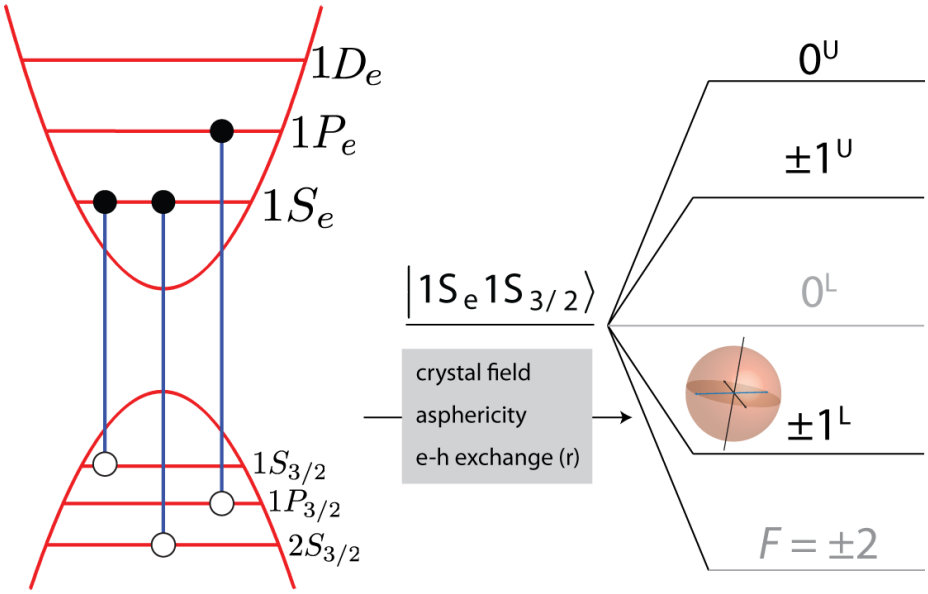

Figure 17. (Left) State diagram of the lowest energy transitions in a CdSe nanocrystal. The band-edge is the $1S_e - 1S_{3/2}$ transition. (Right) Splitting of the $1S_e - 1S_{3/2}$ transition arising from crystal field and exchange splitting, as well as shape defects. The lowest allowed transition, $F = \pm 1^L$, is depicted as its two orthogonal, linearly polarized components in the equatorial disk.

independently access the orthogonal components of the $|1^L\rangle$ transition at room temperature, which is manifested as a discontinuous jump between two emission moment orientations under rotating pump polarization in the x-y plane. The modifications to the nanocrystal electronic structure by the conjugated OPV oligomers, we believe, arise from asymmetrically Stark-modified $|X\rangle$ and $|Y\rangle$ QD states from charge separated ligands. In the case of a pinned charge at the surface of the nanocrystal, these shifts have been calculated to be on the order of 70-75 meV.

4.2 Strong Linear Dichroism in Absorption

Linear dichroism is a measure of the polarization response of a single molecule to a rotating excitation field and has been used extensively to examine the nature of the transition dipole moment in organic chromophores.[73-75] Conjugated organic molecules, which have transition moments polarized along the conjugation axis normally show very strong linear dichroism. These measurements can thus be used to determine the lab-frame orientation of the molecular absorption moment. The modulation depth, given here by $M = (I_{max} - I_{min})/(I_{max} + I_{min})$ where I_{max} (I_{min}) correspond to the maximum (minimum) detector counts in a single polarization rotation, ranges from 0 to 1. Isotropic absorbers, such as dye-doped polystyrene beads containing hundreds of randomly-oriented linear chromophores within a diffraction limited spot, exhibit a negligible modulation depth, while single linear absorbers such as DiI show near-unity modulation depths. Such polarization anisotropy experiments have also been carried out on CdSe/ZnS core-shell nanocrystals by Bawendi and coworkers,[67, 68] showing a modulation depth centered

around M=0.5 for an ensemble of single nanocrystals dispersed in polymethylmethacrylate. This value was attributed to the large collection angle of the high-NA objective used, the intrinsic nanocrystal transition moments, and the modified dipole radiation patterns in the proximity of the dielectric (glass) surface.[68]

In the 2D degenerate picture, the ellipse projected onto the sample plane determines the modulation depth for a single randomly dispersed QD, depicted schematically in the inset of Fig. 18(a). We denote the orientation of the nanocrystal by the polar coordinates (θ, φ) made by the crystal c-axis relative to the z (optic) axis of the experiment. The intensity of excitation (and therefore emission) I_{2D} as a function of (θ, φ) and the angle of the linearly polarized excitation field φ_{ex} is therefore

$$I_{2D} = I_0\left[\cos^2\theta + \sin^2\theta\cos^2(\varphi_{ex} - \varphi)\right].$$

For a single cycle of a polarization anisotropy measurement, the angle φ_{ex} is swept out over 2π radians (although the polar angle θ is not measure directly, it is calculated as discussed below). Figure 18(a) shows traces for two

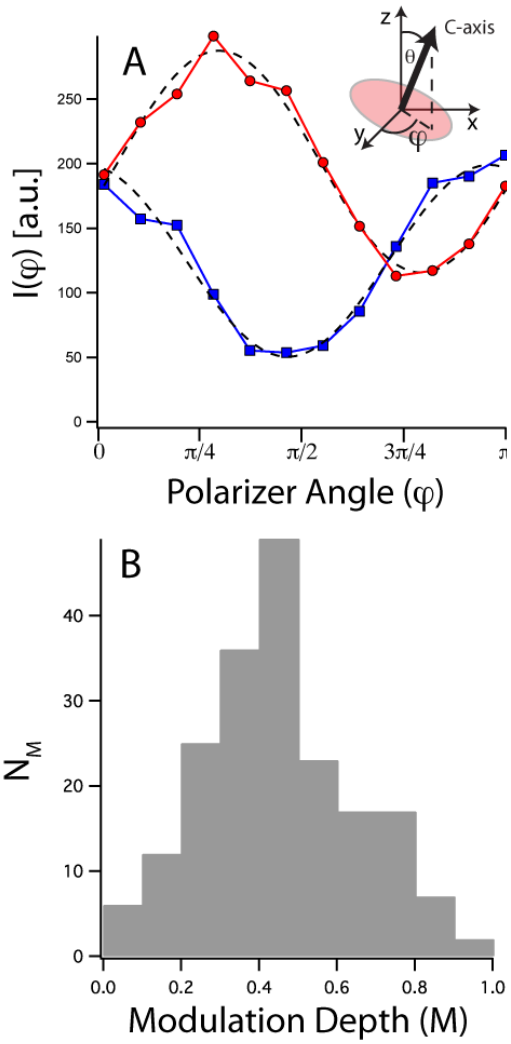

Figure 18. (a) Experimental polarization modulation traces for 2 CdSe-OPV nanostructures. The phase offset of 60° is real, showing no experimental polarization bias. The fitting parameters for each particle are M = 0.58, θ = 59° (●) and M = 0.45, θ = 52° (■). The dashed lines are fits to $\cos^2(\varphi)$ functions. Inset: Schematic representation of a 2D transition dipole moment with normal crystal c-axis at polar angle θ and azimuthal angle φ. (b) Histogram of M parameters for 200 CdSe-OPV nanostructures, with $\overline{M}$ = 0.47.

single CdSe-OPV nanostructures, which are averaged over 10π cycles of the pump polarization to mitigate fluorescence intermittency. M values are obtained by fitting to $a+b\cos^2\varphi$ (dashed lines in Fig. 18(a)) ; from these M values, the orientation of the crystal c-axis is calculated as (see Appendix A)

$$\theta = \sin^{-1}\sqrt{\frac{2M}{1+M}}.$$

The resulting fits for the traces in Fig. 18(a) yield M = 0.58, θ = 59° (●) and M = 0.45, θ = 52° (■). By fitting these parameters, we can accurately determine the lab-frame orientation of the absorption moment of individual nanostructures.

4.3 Linear Dipole Radiation Distribution and Fluctuations in Emission

In addition to probing dichroic PL intensity response with linearly polarized excitation, we sought to probe the nature of the emission moment and its correlation with the excitation directionality. For organic dyes such as Cy5 and $DiIC_{12}$, the absorption and emission moments have been shown to be nearly, but not completely, collinear.[74, 75] Defocused imaging of spatial distributions of emitted photons through high numerical apertures has been used extensively to characterize single molecules[76, 77] and quantum dots[70-72]. By introducing slight spherical aberration, anisotropies in the resulting images contain information on the transition dipole axis (or axes). This technique is useful because it allows for transition moment imaging while simultaneously monitoring photoluminescence dynamics. For single dye molecules, this method has been applied to determine rotational diffusion rates in porous media[78] and to verify modifications in radiative lifetime in relation to emitter orientation[79]. In single quantum dot studies, this

technique has been applied to determine the orientation of the nanocrystal on the substrate surface. In this case, the image resulting from the 2D degenerate disk is the sum of two orthogonal linear dipoles (see Figure 19(a)), although groups have reported success in modeling experimental photon distributions using 3 linear dipoles[71] or a 2D + 1D scheme.[72]

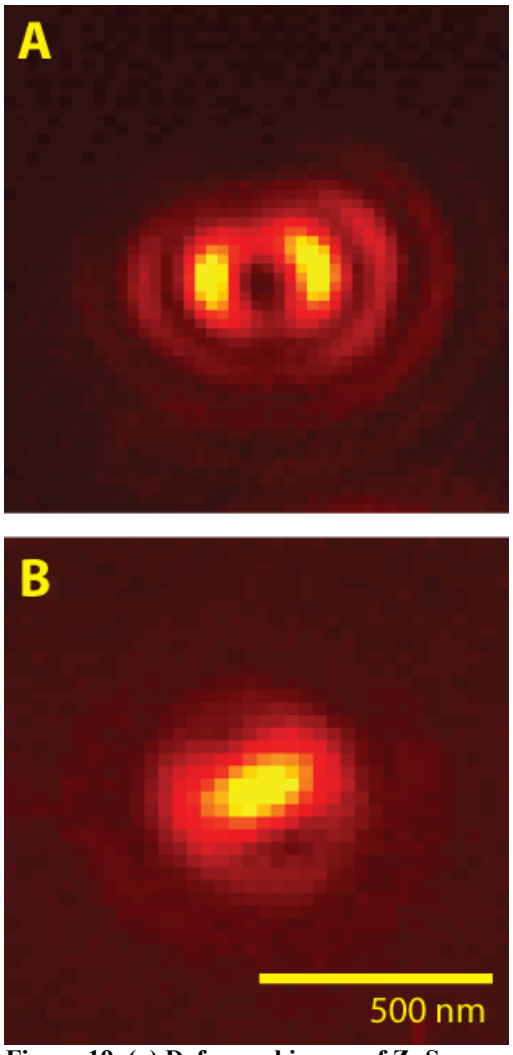

Figure 19. (a) Defocused image of ZnS-capped CdSe QD. The central node and side lobes are indicative of a *2D dipole* with c-axis parallel to the sample plane. (b) Defocused emission pattern of CdSe-OPV, showing a distinct *linear dipole* emission pattern.

Unlike organic chromophores, where the emission dipole is typically fixed, the emission transition dipole of the nanocrystal core in a CdSe-OPV nanostructure displays complex behavior. Figure 19(b) shows a typical defocused emission pattern (DEP) from a single nanostructure with fixed pump polarization characteristic of a linear transition dipole (dipole axis parallel to the major axis). All defocused images were spectrally filtered to exclusively collect emission from the CdSe core. During the linear dichroism runs, the DEP was observed to fluctuate as a function of the pump laser polarization for a significant fraction of the nanostructures imaged (reorientation of the major emission axis). As the samples were cast from THF onto neat glass and dried under

dry N_2 flow, physical reorientation of the nanostructure throughout the course of the experiment is unlikely.

By combining linear dichroic and DEP measurements, we investigate the correlation between the absorption moment, emission moment, and excitation E field for single nanostructures. Figure 20 shows simultaneous time trajectories of both the in-plane emission dipole orientation (a) and the PL intensity (c) from a single CdSe-OPV nanostructure under rotating pump polarization. The dashed line in (c) represents the rotating laser polarization, where the maxima(minima) correspond to V(H) polarization. The transition dipole orientations in (a) were determined by fits to the major axis of the DEP at a defocus depth $\delta z \approx 1000$ nm (toward the sample plane). Figure 20(d) shows the lab-frame phase-averaged emission from the trajectory in (c) along with a sine-squared fit

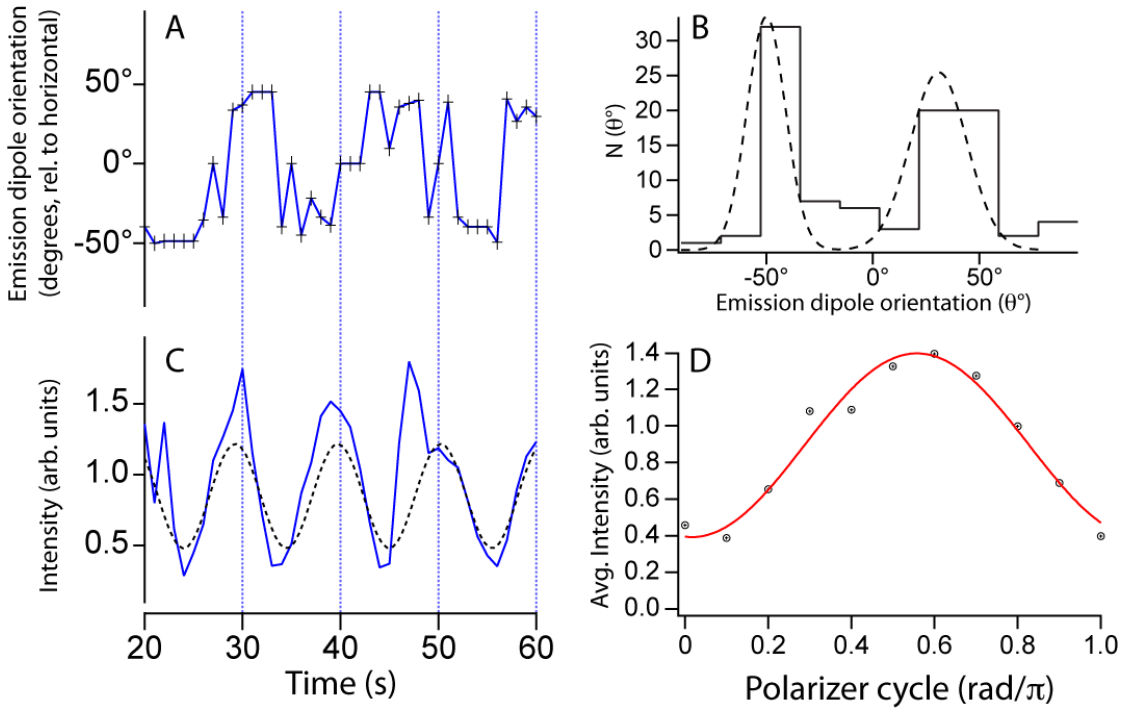

Figure 20. (a) Emission moment trajectory for a single CdSe-OPV under polarizer rotation (shown as dash in (c)) with respect to lab-frame horizontal axis. (b) Histogram of emission moment orientations for 100 s of collection. The Gaussian fits to the two features indicate an angle of 82° between |X> and |Y> axes. (c) Intensity trajectory for the same particle; the dashed line indicates the excitation polarization (see text) (d) Intensity for a single polarizer cycle averaged over 10 cycles (points), along with a $\cos^2\varphi$ (solid line). Corresponding fitting parameters are M = 0.57, θ = 58°.

(dashed line). Comparison to a histogram of lab-frame emission orientations over 100 seconds in Fig. 20(b) shows two discrete linear emission orientations at roughly 45° and -50°, which correspond to the maximum and minimum absorption points in the phase-averaged emission curve. The discontinuous 'jump' between two distinct orientations of the transition moment orientation was typical of the nanostructures displaying this behavior. The nanostructure shown in Figure 20 exhibits such a jump from -50° to +50° (with respect to the horizontal axis) between t = 23 s and t= 30 s, after which it immediately returns to the previous mean value. As indicated in figure 20, the jumps in emission orientation do not follow the laser polarization directly for the nanostructure, but rather "lag" the excitation field in time for 1-2 seconds. This was observed in almost all of the CdSe-OPV particles sampled.

4.4 Wavelength-dependent Intensity Autocorrelation Functions

To further verify the electronic interaction of surface ligands with the polarization properties of the CdSe core, we examined the linear dichroic and DEP behavior of CdSe-OPV using 514 nm excitation, where ligand absorption is negligible. While the absorption profiles of CdSe and the OPV ligands do not permit exclusive excitation of each moiety individually, excitation near the CdSe band edge completely avoids ligand excitation. In this way, the behavior of the hybrid system without ligand excitation is interrogated. Photoluminescence from single nanostructures was spectrally filtered to monitor QD emission strictly. At this wavelength, fluorescence intermittency becomes pronounced, providing further support for the role of photoexcited ligands in blinking suppression reported earlier.[21] The linear dichroism observed at 405 nm becomes less

pronounced at 514 nm, and is complicated by the increased blinking at this wavelength. We make use of autocorrelation analysis to probe linear dichroism signatures that avoid these complications.

Figure 21 shows intensity trajectories *I(q)* and corresponding autocorrelation functions *C(g)* for single CdSe-OPV nanoparticles illuminated at 405 nm (Fig. 21(a), 21(b)) and 514 nm (Fig. 21(c), 21(d)) over a 4π rotation of the excitation electric field. The dashed lines indicate the lab-frame electric vector in the X-Y plane (maxima (minima) correspond to V(H) polarization). Autocorrelation analysis was performed to identify periodic fluorescence intensity peaks while simultaneously averaging over short dark periods. The linear polarization-dependent discrete intensity autocorrelation

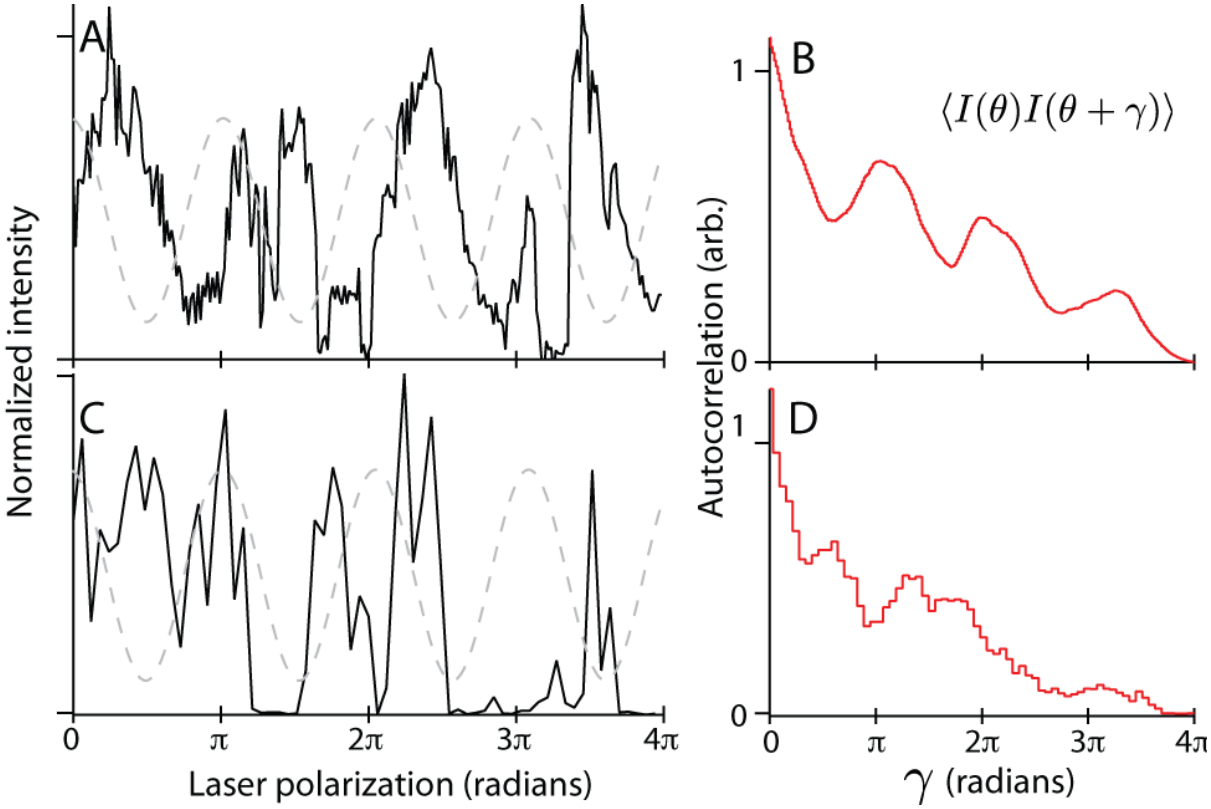

Figure 21. (a) Intensity trajectory (solid) as a function of laser polarization (dashed; maximum (minimum) corresponds to V(H) polarization) under 405 nm (ligand + QD) excitation. (b) Intensity autocorrelation C(γ) for the trace in (a), showing clear maxima at π intervals. (c) Intensity trajectory and laser polarization under 514 nm (QD only) excitation. (d) Corresponding autocorrelation analysis for the trajectory in (c). The structure in C(γ) arises from fluorescence bursts, with no features at π.

functions are given by

$$C(\gamma) = \sum_{\theta} I(\theta) \bullet I(\theta + \gamma),$$

where $I(\theta)$ is the measured fluorescence intensity at a given electric field orientation, and γ is a stepped polarization offset. For linear absorbers with intensity maxima $I(\theta)_{max} \sim \cos^2 \theta$, this results in maxima in $C(\gamma)$ at intervals of π, which is clearly seen in Fig. 21(b) under 405 nm excitation. The intensity trajectory in fig. 21(a), taken using 100 ms integrations over 250 frames, shows discrete fluorescence intermittency superimposed on a $\cos^2 \theta$ polarization response. From this, the lab frame orientation of the absorption dipole moment can be obtained, although this information is not needed for these comparisons.

Both the intensity trajectories and autocorrelation functions for individual CdSe-OPV nanostructures showed distinct differences under 514 nm excitation compared with 405 nm. The intensity trajectory in fig. 21(c) consists of 65 1-second integrations over a 4π electric field rotation. The fluorescence intensity required 10X binning due to the significantly lower absorption at this wavelength, characteristic of 'bare' ZnS- or TOPO-capped CdSe QDs. The autocorrelation features are not present at p intervals, which indicates a lack of linear polarization response to the rotating field. The observed structure in $C(\gamma)$ arises from the fluorescence bursts and is not related to the polarization response. This was common for nearly all of the observed nanostructures.

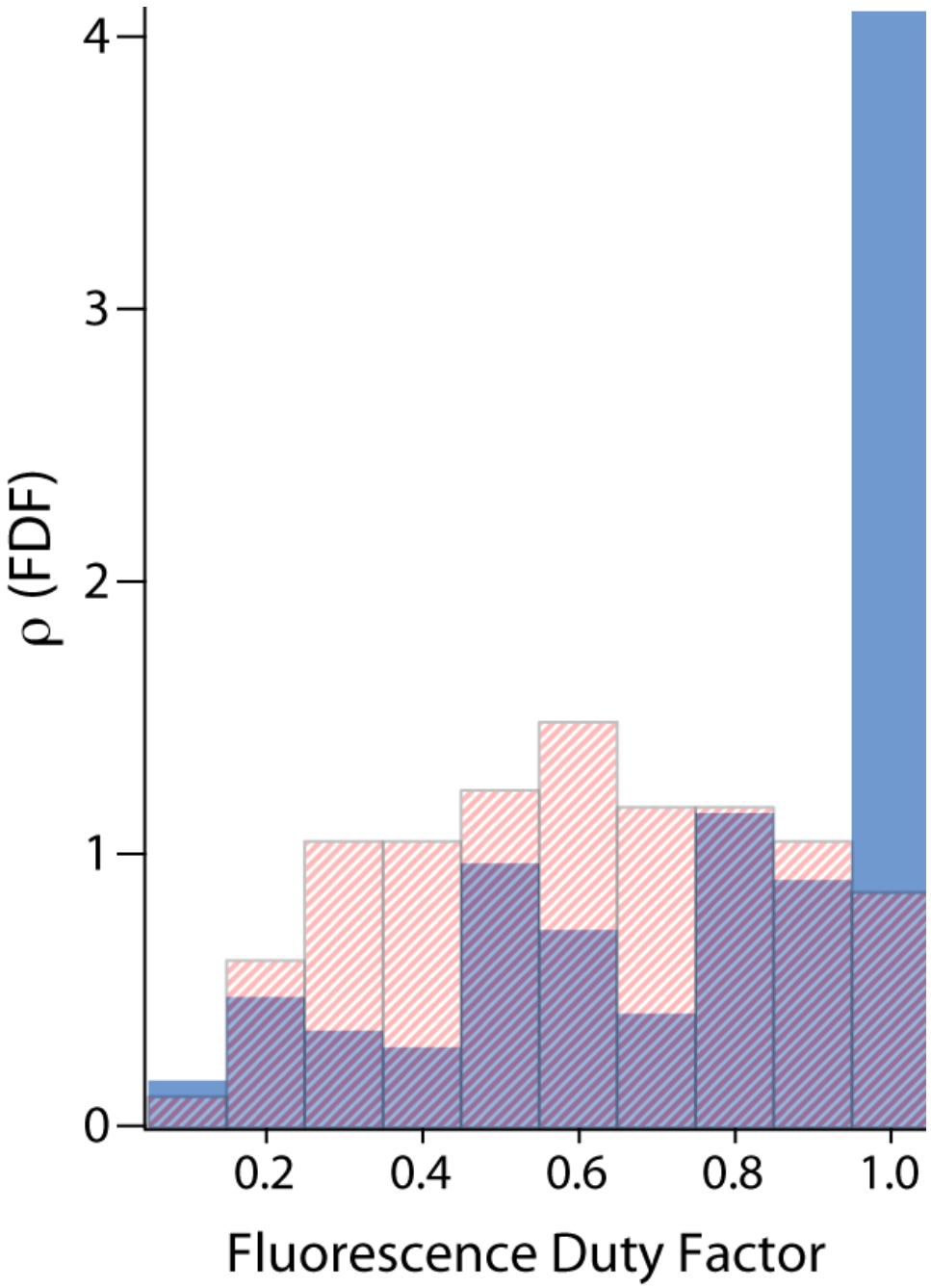

Figure 22. Histograms of fluorescence duty factors (% time 'on') under 405 nm (ligand + QD; solid bars) and 514 nm (QD only; dashed bars) excitation. The average computed FDFs were 0.74 (405 nm; sample size 163 nanostructures) and 0.60 (514 nm; 160 nanostructures).

To quantify the intermittency, we computed fluorescence duty factors (FDFs), which correspond to the percentage of the total experiment time a single nanostructure spends above a 2s noise threshold ('on' state), at both 405 nm and 514 nm excitation

wavelengths. Although these quantities have the disadvantage of being inherently dependent on both total experiment time and time binning *dt*, the suppressed blinking in these hybrid systems renders traditional 'power law' blinking statistical analysis extremely difficult, hence motivating statistical analysis through both autocorrelation and FDFs. Histograms of these FDFs are shown in Figure 22. To accurately compare the two FDFs, data collected using 405 nm excitation were rebinned 10X from 100 ms up to 1 sec. The dashed bars show the normalized histogram of FDFs from 160 CdSe-OPV nanostructures under 514 nm excitation, with an average value $\langle \mathrm{FDF} \rangle_{514\,\mathrm{nm}} = 0.60$. This largely unstructured distribution of FDFs is similar to that measured in this lab for ZnS-capped QDs[21]. The solid bars show the FDF distribution for 163 CdSe-OPV nanostructures excited at 405 nm (ligand + QD) with $\langle \mathrm{FDF} \rangle_{405\mathrm{nm}} = 0.74$. This measured distribution is strongly peaked near 1, indicating a large degree of blinking suppression at this wavelength.

It is clear from these data that the role of the photoexcited ligands is central to the observed modification in photophysical behavior for CdSe-OPV. Exciting the hybrid system to the red edge of the ligand absorption band results in fluorescence behavior similar to both CdSe/ZnS and CdSe-TOPO, including long excursions into dark states and largely degenerate 2D absorption behavior at thermal temperatures. By tuning to the tailing edge of the ligand absorption band, we gain access to a high degree of blinking suppression and highly linear absorption behavior. We believe the cause of this abrupt change in fluorescence properties at these wavelengths arises from photoinduced charge separation in the surface-coordinated oligomers, which is only accessed at higher photon energies. These effects are discussed below.

4.5 Discussion

The small (~3 meV) splitting observed between the $|X\rangle$ and $|Y\rangle$ states in CdSe/ZnS nanocrystals at cryogenic temperatures observed by Htoon *et al.*[14] is greatly enhanced by the presence of the OPV oligomers at the nanocrystal surface in the present experiments. The subset of ligands efficiently excited at a given pump polarization (proportional to $|E\|\mu|\cos\theta$, with θ the angle between the pump polarization and oligomer transition moment $\boldsymbol{\mu}$) generates excitons in the organics localized near the nanocrystal surface. The difference in electronegativities between QD and semiconductor organic layer[80] drives electron transfer from ligand to QD across the saturated P-O linker, resulting in charge separated oligomers with a static charge distribution.

To get an estimate of the expected Stark shifts in CdSe-OPV, the electric field *E(r)* in the nanocrystal interior due to a single charge separated oligomer was calculated as[81]

$$E(r) = \frac{3}{[\varepsilon_{NC}/\varepsilon_0 + 2]} \frac{q}{4\pi\varepsilon_0} \left[\frac{1}{r^2} - \frac{1}{(r+\alpha)^2} \right]$$

where r is the distance from the nanocrystal surface, $\varepsilon_{NC}/\varepsilon_0$ is the ratio of dielectric constants of CdSe (taken to be 6 from Guyot-Sionnest *et al.*[82]) and free space, q is a unit charge, and a is the ligand length. The screening effect of the hole remaining localized on the ligand is included in the parameter a. This results in large internal fields near the coordinated ligand, which are on the order of 10^3 kV/cm at the nanocrystal interior. Comparison to bulk measurements by Empedocles *et al.*[83] show that these field strengths are more than sufficient to cause Stark shifts on the order of 75-100 meV along the

polarizable axis of the photoexcited ligand. In Chapter 5, perturbation theory calculations are detailed which predict shifts of this magnitude without the use of empirical data from bulk measurements.

Pseudopotential calculations by Wang[84] on the effects of pinned charges near the QD surface support the above observations. The presence of a localized charge near the coordination site of the OPV ligand, generated by photoinduced charge separation when the organic excitation is efficiently driven, causes coulombic separation of the internal QD electron and hole wavefunctions, and hence strong degeneracy breaking between $|X\rangle$ and $|Y\rangle$ states) along the axis defined by the conjugated ligand backbone. The rotation of the laser electric field in the X-Y plane sequentially excites ligands with a large projection of their transition moments onto the laser electric vector, resulting in the fluctuation in emission moment described above. This effect is not as obvious in absorption, where intermittency and shot noise obscure secondary structure in the polarization anisotropy measurements.

In conclusion, we have studied the modified transition dipole moment characteristics of CdSe-OPV nanostructures using both polarization anisotropy and defocused widefield imaging techniques. These nanostructures exhibit the absorption characteristics of essentially 2D degenerate absorbers randomly distributed in a plane, albeit with a higher-than-expected average modulation depth ($\overline{M}_{\text{obs}} = 0.47$) compared to that predicted for an ideal, randomly distributed ensemble of 2D degenerate absorbers. However, the observed emission dipole transition obtained from widefield imaging appears as a fluctuating linear transition moment, which until now has not been observed in these so-called 2D degenerate systems. These effects are greatly diminished when the

excitation wavelength is tuned away from the absorption band of the conjugated organic ligands coordinated to the QD surface. We attribute this effect to a large ligand-induced splitting of the orthogonal equatorial transition moment components. This splitting arises from a directional Stark shift from localized charges generated in the organic capping layer. This work presents an important first step toward the incorporation of single colloidal nanocrystal structures into device applications, where directionality in control is crucial.

CHAPTER 5

POLARIZATION-DRIVEN STARK SHIFTS IN QUANTUM DOT LUMINESCENCE FROM SINGLE CdSe-OPV NANOSTRUCTURES

5.1 Introduction

Understanding energy and charge exchange processes in nanostructured materials is critically important for development of high-efficiency optoelectronic devices. Surface-functionalized quantum dot (QD) systems with semiconducting organic materials offer an interesting material format to explore such interactions, where the molecular architecture and choice of ligands can be used to manipulate spatial, temporal, and spectral properties of the QD luminescence.[14, 21, 85] Recent studies have shown that ligands with electron-donating character can have profound effects on fluorescence intensity fluctuations (blinking) and photostability in isolated QD systems.[33, 34] In similar systems where surfactants have been used to facilitate charge transfer between nanocrystals and organics, strong modification of QD photoluminescence intensity fluctuations (blinking suppression) have been observed.[86] These observations seem to point to a common mechanistic origin; namely that enhanced charge density near the surface of the QD can profoundly affect QD luminescence properties. However, definitive evidence linking excess surface charges to modified QD luminescence has not been shown.

Here we report observation of polarization-resolved spectral shifts ($\Delta E \approx -70$ meV) from individual CdSe QDs surface-functionalized with monodisperse *oligo*-(phenylene vinylene) ligands (CdSe-OPV). We show that both the observed spectral shift and linear

polarization can be quantitatively described by a screened electrostatic (Stark) polarization of the QD electron-hole wavefunction from a single point-charge, providing compelling evidence for a charge-separation mechanism for excited state quenching in the organic surface ligands. These observations suggest the potential of using emission energy and luminescence polarization from single CdSe nanocrystals as local probes of mobility of nearby charge carriers.

The CdSe-OPV NP system is a hybrid inorganic/semiconducting organic structure which appears to retain photophysical properties of both the QD core *and* the organic ligand. Fluorescence emission spectra from individual CdSe-OPV nanoparticles (NPs) is characterized by almost complete extinction of the organic ligand fluorescence – greater than 99% of the fluorescence intensity is carried by the band-edge luminescence of the QD, [20] along with blinking suppression, and enhanced spectral stability relative to TOPO -capped QDs.[21] Observation of photon antibunching from single CdSe/OPV NPs (>75% modulation at $\Delta\tau = 0$) confirmed that the novel polarization and blinking suppression derives from surface-modified QD photophysics and gives further evidence for strong OPV-QD interactions resulting in single-fluorophore behavior.[24] In addition, we recently reported a surprising *linear* polarization in both absorption and emission from individual CdSe-OPV NPs.[25, 26] While linear polarized luminescence has observed in CdSe nanorods[85] where strong exciton confinement exists in only one dimension), or in prolate nanocrystals at low temperature (where the shape distortion lifts the degeneracy of orthogonal X-Y Bloch components in the QD wavefunctions),[14] the CdSe-OPV system preserves a spherical symmetry as implied by AFM and DLS structural studies. We speculated that the observed linear dichroism in absorption ($< M > \approx 0.6$) and distinct

linear dipole emission patterns derived from an enhanced absorption cross section of the hybrid system at excitation polarizations that overlap with the ligand conjugation axis. Exciton dissociation within the *organic* ligand, followed by electron trapping near the QD surface[26] offered an attractive heuristic explanation in that it qualitatively accounted for the quenching of the organic luminescence, and the linear dipole character.

This mechanism should have a clear experimental signature in the alteration of electron and hole energies from the Stark interaction from the electric field generated from a point-charge near the surface of QD such that the apparent recombination energy is lowered. Here we report on measurements of spectral shifts of band-edge luminescence from single CdSe-OPV NPs correlated with a specific polarization angle of the excitation source. We observed red shifts greater than 70 meV (peak to peak) for excitation polarizations corresponding to maximum luminescence intensity, compared to the ≈10 meV random spectral diffusion observed in ZnS-capped quantum dots of similar core radius. These observations are supported by perturbation calculations of the Stark-induced wavefunction distortion, spectral shifts, and induced linear polarization. First-order corrections to the QD $1S_e$ electron and $1S_{3/2,M}$ hole energies and wavefunctions arising from a trapped charge at the QD surface account quantitatively for both the spectral shifts and polarization anisotropy observed in single CdSe-OPV NPs. These combined results strongly support an exciton dissociation mechanism in the organic ligands, where the electric field from the electron near the QD surface drives a Stark shift of the QD band-edge energy, as well as a strong linear polarization along the axis connecting the excess charge and the QD center. Modulation of the pump polarization acts as the initiator of the Stark field, which appears as a slowly varying DC field on the

spectral integration and polarization rotation time scales required for single-particle spectral measurements.

5.2 Correlated Absorption and Emission Orientations in Single Particles

Samples coverslips were prepared by sequential sonication in acetone, ethanol, methanol, and alkali detergent (Micro-90, Cole Parmer), rinsing with deionized water, and drying with a dry nitrogen flow. All experiments were performed on neat glass. As a control, a nanomolar solution of commercial CdSe/ZnS QDs (evidot 600, Evident Technologies) in toluene was spincoated at 3000 RPM directly onto coverslips. For experiments on CdSe/OPV NPs, a nanomolar solution of CdSe/OPV in dry tetrahydrofuran was deposited onto cleaned cover slips and dried under N_2. CdSe/OPV NPs were synthesized as previously reported.[25] Briefly, CdSe-TOPO nanocrystals were synthesized by literature methods,[9] and subsequent ligand exchange reactions with *oligo*-(phenylene vinylene) ligands containing a di-*n*-octylphosphine oxide group yielded highly monodisperse nanostructures, as measured by dynamic light scattering and AFM surface height measurements.

Figure 23(a) shows a schematic of the experimental setup. Samples were excited using wide-field epi-illumination using a lens (WL) to focus a continuous wave 405-nm diode laser at the back aperture of a 1.4NA, 100x microscope objective (OBJ). Laser light transmitted through the sample was focused through a linear polarizer (POL) onto a photodiode (PD) to record the laser polarization (rotated using a half-wave ($\lambda/2$) plate); this technique was reported by Jung *et al.*[87] for interrogating rotational dynamics of chromophores in confined matrices. In these experiments, the $\lambda/2$ plate was rotated using

a mechanical rotation stage (Newport 8401 with Picomotor driver), limiting polarization modulation speeds to ~2π rad/ 7 sec. A 435-nm long-pass dichroic mirror (DC) and 530-nm long-pass emission filter (LP) were used to filter out residual laser scatter and sample autofluorescence. Particle fluorescence was collected through the same objective, focused using a 200-mm tube lens, and routed to either a high-speed imaging CCD or to a spectrograph/high-aspect ratio CCD for spectral measurements. In all cases, single QD photoluminescence intensity scaled linearly with excitation intensity, ensuring that we avoided any complications arising from multiexciton generation. Spectra were recorded using 2-second exposures with a resolution of 0.6 meV/pixel. We used a multichannel data acquisition (DAQ) board (National Instruments) to synchronize the CCD camera exposures with polarization measurements.

Figure 23(b) shows a sample widefield image of several CdSe-OPV NPs under slight (~600 nm) defocusing. Defocused emission pattern imaging is now a commonly-used method for the determination of molecular transition dipole moment orientation; fluorescent systems with single (linear) dipole character show distinct patterns defined by the dipole orientation in θ and ϕ.[69, 77, 78] As previously observed,[26] the emission from single CdSe-OPV NPs show the characteristic dipole pattern for an in-plane linear dipole (signified by arrows for particles i and ii). Because we are interested only in the in-plane orientation in these measurements, we approximate the central bright axis of the defocused emission patterns (such as those in fig. 23(b)) by an ellipse composed of two orthogonal Gaussian functions with major axis at an angle θ with respect to the lab-frame vertical axis

$$F(x,y) = A \cdot \exp\left[-\left(\left(\frac{\cos^2(\theta)}{2\sigma_x^{\,2}} + \frac{\sin^2(\theta)}{2\sigma_y^{\,2}}\right)(x-x_0)^2 + 2\left(\frac{-\sin(2\theta)}{4\sigma_x^{\,2}} + \frac{\sin(2\theta)}{4\sigma_y^{\,2}}\right)(x-x_0)(y-y_0) + \left(\frac{\cos^2(\theta)}{2\sigma_x^{\,2}} + \frac{\sin^2(\theta)}{2\sigma_y^{\,2}}\right)(y-y_0)^2\right)\right],$$

where A is the amplitude, x_0 and y_0 are the centroid coordinates, and σ_x and σ_y are the x and y widths. This yields emission dipole moments -42° and +73° with respect to the vertical polarization axis for molecules (i) and (ii) respectively. Defocused emission

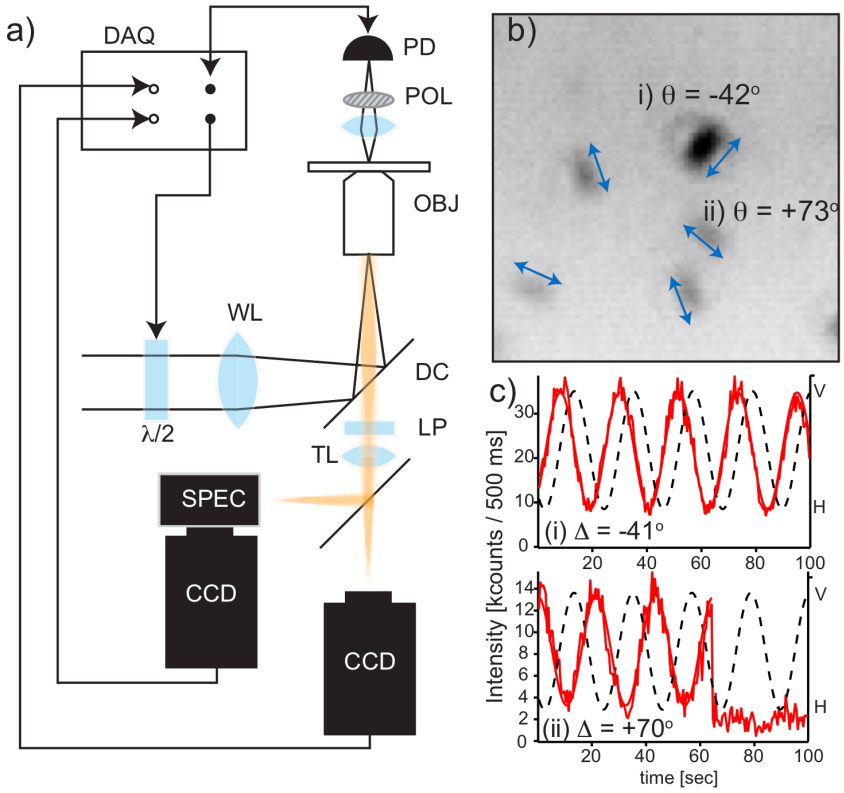

Figure 23. (a) Experimental setup. See text for details. Polarization modulation is controlled via half wave plate (l/2) and monitored in transmission through a polarizer (POL) and photodiode (PD). Polarization rotation and monitoring are synced with camera exposures via data acquisition (DAQ) board. (b) Summed widefield image of CdSe-OPV under slight defocusing; arrows show approximate transition dipole orientation. Fit orientation for particles (i) and (ii) are -42° and +73°, respectively. (c) Polarization trajectories for particles (i) and (ii) along with laser polarization (dashed line). Phase offsets are given, showing good agreement with widefield results.

patterns were fit after summing all fluorescence images and subtracting background pixel counts. Differences in particle intensity in the widefield image arise from fluorescence intermittency and bleaching during the experiment.

For these same particles, fluorescence intensity trajectories were recorded under rotating pump polarization, showing strong polarization anisotropy in absorption, also consistent with our earlier reports.[26] Figure 23(c) shows polarization trajectories for the two particles, along with the laser polarization (ranging from vertical to horizontal, dashed lines). Particles (i) and (ii) modulate with phase offset angles of -41° and +70° respectively, which we obtain by comparing the phase offset term Δ in a fit to $A+B\cos^2(\omega x+\Delta)$ for the transmitted laser polarization and the CdSe-OPV fluorescence anisotropy signal. Abrupt photobleaching is evident in the fluorescence signal for particle (ii), evidence of the single-emitter nature of CdSe-OPV NPs. The small difference in orientation determination from the two methods could arise from error in the image fitting procedure, which we estimate to be 2-5° depending on fluorescence signal levels. However, small offsets in the absorption and emission transition dipoles of organic dyes have been reported in similar studies and were attributed to inverted lab-frame molecular conformations on the sample surface.[74] We note here that significant information could be gained in the temporal response from single particles to polarization modulation on fast time scales (comparable to the relaxation time of the charge separated organic state), analogous to amplitude modulation experiments. Future experiments utilizing faster polarization modulation hardware (i.e. computer-controlled EOMs) are planned to probe this temporal response.

5.3 Pump Polarization Effects on CdSe/ZnS and CdSe-OPV Nanostructures

To explore the effect of pump polarization on emission energy in CdSe-OPV, the same setup was used to collect sequential emission spectra (spectral traces) from single nanostructures over long periods under constant rotation of the laser electric field. Sequential spectra were fit to single Lorentzians using an automated routine to determine center position, amplitude, and width. Figure 24(a) and 24(b) show spectral traces from single CdSe/ZnS and CdSe-OPV nanostructures with slowly varying laser polarization. The emission peaks are marked with red (blue) markers for CdSe/ZnS (CdSe-OPV), and the laser polarization (measured in transmission using a polarizer and photodiode) is represented alongside each spectral trajectory. Clearly, the emission spectra of CdSe/ZnS appear insensitive to pump polarization, with blinking events occurring at various pump polarization angles. In contrast, the CdSe-OPV nanoparticle in fig. 24(b) undergoes large, reversible spectral shifts on the time scale of the laser polarization rotation. To quantify this response, we compared fluctuations in the peak emission energies of the two particles.

Figure 24(c) shows a histogram of center emission energies for the two particles, where N(E) are the number of occurrences of a given peak emission energy. For the sake of comparison, the histograms for CdSe/OPV and CdSe/ZnS have been overlaid (the CdSe/ZnS histogram is shifted from its peak position $\langle E \rangle = 2.086$ eV; the width of the histograms appears invariant to center emission energy for all the data collected here). CdSe/ZnS emission energies show very little dependence on pump polarization, which is reflected in the narrow emission peak histogram (12.5 ± 0.3 meV FWHM, red). In comparison, the spectral trajectory for CdSe/OPV shows large fluctuations under rotating

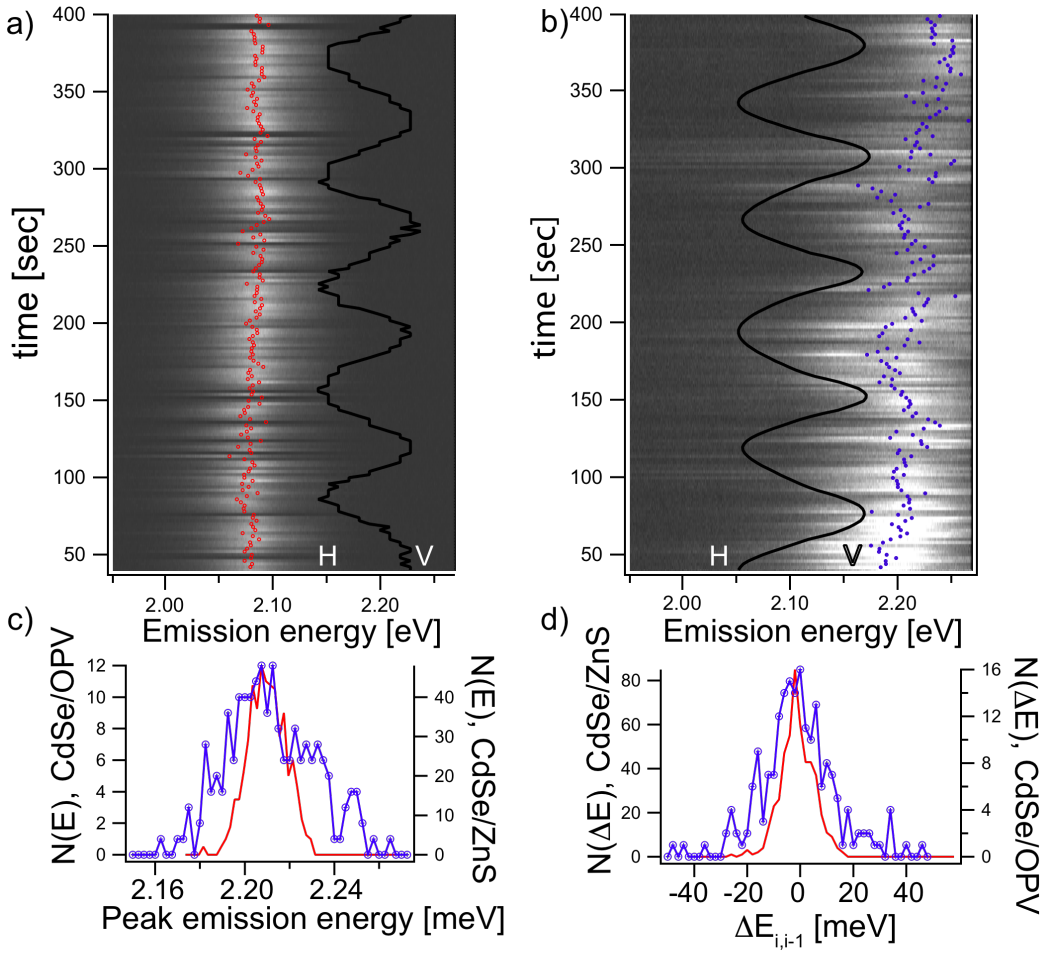

Figure 24. (a) Spectral trace of a single CdSe/ZnS QD over ~360 seconds with fitted peak positions marked in red. Exposure time was two seconds. (b) Spectral trace of a single CdSe/OPV NP under the same conditions. Laser polarization is shown in both traces by the solid black curve. (c) Histograms of peak positions for the CdSe/ZnS QD in (a) (red line, right axis) and the CdSe/OPV nanostructure in (b) (blue lines/markers, left axis). The histograms are superimposed to show the differences in width. (d) Histograms of the energy difference between sequential emission peaks for CdSe/ZnS (red line, left axis) and CdSe/OPV (blue line/markers,

laser polarization. The emission energy histogram is nearly double the width (28 ± 3 meV) of CdSe/ZnS, typical for most particles in the experiment. In extreme cases, energy fluctuations of 70 meV are seen for single particles. Figure 24(d) shows a histogram of the energy difference between sequential emission peaks, denoted by $N(\Delta E_{i,i-1})$ (where i denotes the index of the emission spectrum peak) for the CdSe/ZnS QD (red line) and CdSe/OPV NPs (blue line/markers) shown in fig. 24(a) and 24(b). This analysis has been

used in single QD[31] and nanorod[88] experiments to characterize the sign and magnitude of sequential spectral jumps and spectral jitter. In this histogram, it is clear that spectral jumps greater than 20 meV are very rarely seen in CdSe/ZnS QDs when irreversible spectral blue shifting is absent. However, the probability of observing jumps in excess of 40 meV in the CdSe/OPV NP, while small, remains finite. These large spectral jumps likely arise from abrupt non-radiative recombination of the charge-separated organic exciton. It is interesting to note that, to a good approximation, both the CdSe/ZnS and CdSe-OPV histograms in Fig. 24(d) are well fit to Gaussian curves, suggesting that the potential surface along which the emission energy diffuses is approximately parabolic. Inverting these distributions to explore the sampled band gap surfaces is an ongoing study.

Figure 25(a) shows peak emission energies from a single CdSe-OPV NP (top, red lines/markers) and a CdSe/ZnS QD (middle, blue line) as a function of slowly varying laser polarization (bottom) obtained using the same microscope configuration to collect sequential emission spectra (spectral trajectories) from single NPs. Similar experimental setups have been used to study DC Stark shifts,[83] zero-phonon lines,[89] and discrete spectral events[31, 90] in single QDs at low temperature, and irreversible blue shifting[91, 92] at room temperature. Sequential spectra were fit to a single Lorentzian function using an automated routine to determine center position, amplitude, and width, and data were manually checked to exclude contributions from particles showing irreversible blue shifting. For both particles, the average emission energy is superimposed on the trajectory, and the average energy of the CdSe/ZnS QD has been red-shifted by 70 meV for easier comparison with CdSe-OPV. The emission energy fluctuations of CdSe/ZnS appear largely insensitive to laser polarization and exhibit a

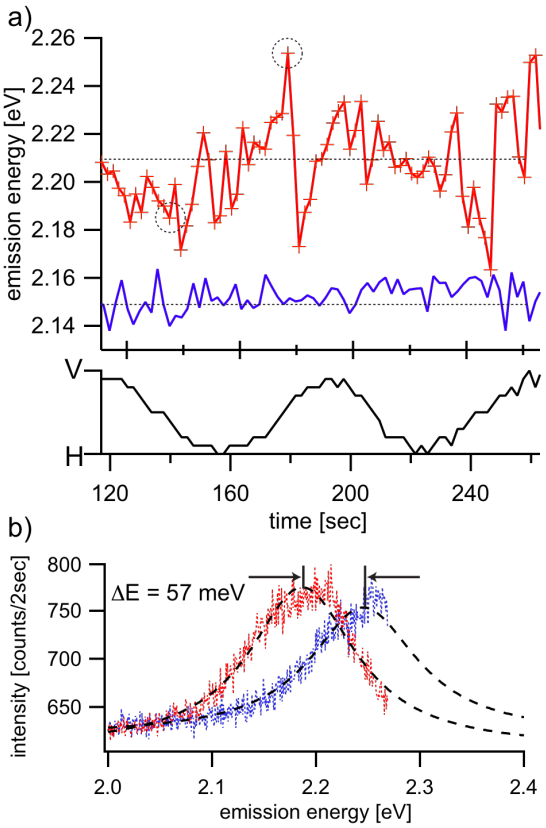

Figure 25. (a) Peak emission energy vs. laser polarization for a CdSe-OPV NP (top, red lines/markers) and a CdSe/ZnS QD (middle, blue), with dashed lines showing average energy. Laser polarization is shown on bottom. CdSe/ZnS energies are offset by 70 meV for comparison. (b) Emission spectra for CdSe-OPV at the positions marked in (a) corresponding to orthogonal laser polarization, with Lorentzian fits. Peak emission shift is 57 meV.

narrow range of values, characteristic of normal spectral diffusion in single nanocrystals.[51] A histogram of peak energies (see fig. 24) gives an average emission peak ε_{avg} = 2.086 eV with a full width half max (FWHM) of 13 meV, consistent with previous reports.[93] In contrast CdSe-OPV shows large, reversible fluctuations in emission (ε_{avg} = 2.209 eV, FWHM = 28 meV). Figure 25(b) shows two full emission spectra with Lorentzian fits from the CdSe-OPV trajectory in fig. 25(a) at the positions marked (t=140 s and t=180 s), corresponding to approximately orthogonal excitation polarizations. The spectral cutoff at the low-energy edge of the spectrum is the result of the finite wavelength range of the spectrograph/CCD array. The measured spectral shift between the two peaks is 57 meV, with shifts as large as 70 meV observed in single CdSe-OPV NPs. Shifts of this magnitude are seen only under rotating laser polarization, which otherwise undergo standard spectral diffusion. Larger amplitude shifts are present in the CdSe-OPV trajectory in fig. 25(a) that do not occur at orthogonal excitation polarizations. We speculate that these sudden jumps arise from non-radiative recombination of organic excitons, which complicates the analysis of the experimental dependence of the Stark shift on pump polarization. The broadened spectral width can be attributed to charge dynamics that are fast on the time scale of polarization modulation, which are discussed below.

5.4 Perturbation Calculations to Exciton Wavefunctions

In previous work, we proposed that linear dichroism in CdSe-OPV NPs derived from the formation of trapped surface charges.[26] Excitations generated in the coordinated organics attached to the surface of the CdSe QD are strongly polarized along the

conjugation axis of the ligand. Due to the alignment of CdSe electron/hole levels and OPV HOMO-LUMO gap, the proximal CdSe QD acts as an electron sink,[5, 94] generating a driving force for dissociation of the organic exciton and transfer of the electron to the QD surface. This results in a long-lived (~800 μs) polaron in the OPV ligand.[95] The resulting electron trapped near the QD surface generates an electric field which perturbs the envelope wavefunctions of the photogenerated electron and hole in the quantum dot. This perturbation mixes the lowest-lying $1S_e$ and $1P_e$ electron levels as well as the (highest-lying) $1S_{3/2}$ and $1P_{3/2}$ hole states, effectively lowering the QD band edge energy. This also results in a net displacement of the electron and hole wave functions along the axis defined by the charge, increasing the magnitude of transition dipole moment.

5.4.1 Stark Shifts

To model the spectral shifts and linear polarization, we computed the first order Stark corrections to the $1S_e$ and $1S_{3/2,M}$ electron/hole wavefunctions[10] using an operator adaption of the Coulomb interaction energy function between a fixed point charge q at a distance S from the QD surface, and the electron/hole within the QD, as discussed by Wang.[84] The relevant matrix element for the fixed-charge/electron interaction is

$$\left\langle V_e^{(1)} \right\rangle = \frac{q\,e}{4\,\pi\,\varepsilon_0}\frac{3}{S^2(2+\gamma)}\left\langle 1S_e \mid r\cos[\theta] \mid 1P_e \right\rangle$$

where γ is a QD-size dependent screening constant (taken here to be equal to 5.5 from Wang *et al.*[96]). The correction to the $1S_e$ energy was computed as

$$\delta_{1S_e} = -\frac{\left\langle V_e^{(1)} \right\rangle^2}{\Delta E_{1Se,1Pe}}$$

using a value of 0.42 eV for the energy difference between $1S_e$ and $1P_e$ electron levels. The hole states are each 4-fold degenerate, corresponding to M = ± 3/2, ± 1/2 projection of spin angular momentum onto the z-axis. The $1S_{3/2,M}$ wavefunctions therefore take a slightly different form, depending on the choice of M; in general, these states contain higher spherical harmonics, and the interaction energies require two integrals:

$$\left\langle V_h^{(1)} \right\rangle = -\frac{q\,e}{4\,\pi\,\varepsilon_0}\frac{3}{S^2(2+\gamma)}\left\langle 1S_{3/2,M} \mid r\cos[\theta] \mid 1P_{3/2,M} \right\rangle ;$$

$$\left\langle V_h^{(3)} \right\rangle = -\frac{q\,e}{8\,\pi\,\varepsilon_0}\frac{7}{S^4(4+3\gamma)}\left\langle 1S_{3/2,M} \mid r^3\left(-3\cos[\theta] + 5\cos^3[\theta]\right) \mid 1P_{3/2,M} \right\rangle$$

The corrections to the hole wavefunction and energy were computed using a value of 0.05 eV for the energy difference between $1S_{3/2}$ and $1P_{3/2}$ hole levels. Figure 26 shows the calculated magnitude of the Stark shift as a function of charge distance from the surface for a QD. Comparison with our experimental Stark shifts (~50-70 meV) suggests a cycle-averaged distance of ≈ 1.4 nm separating the charge and the QD surface. We note here that these values for the Stark shift are consistent with the values calculated empirically in Chapter 4.

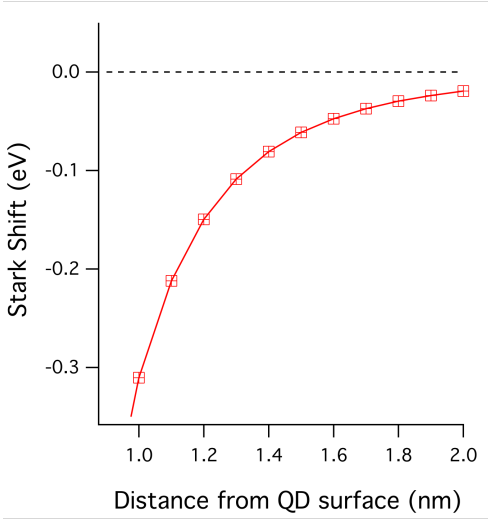

Figure 26. Calculation of the Stark shift magnitude as a function of charge proximity to the QD surface.

5.4.2 Linear Transition Dipole Moment

Figure 27 shows the computed $1S_e$ and $1S_{3/2,M=+3/2}$ electron and hole states perturbed by a fixed electron 1 nanometer from the dot surface. Qualitatively, these

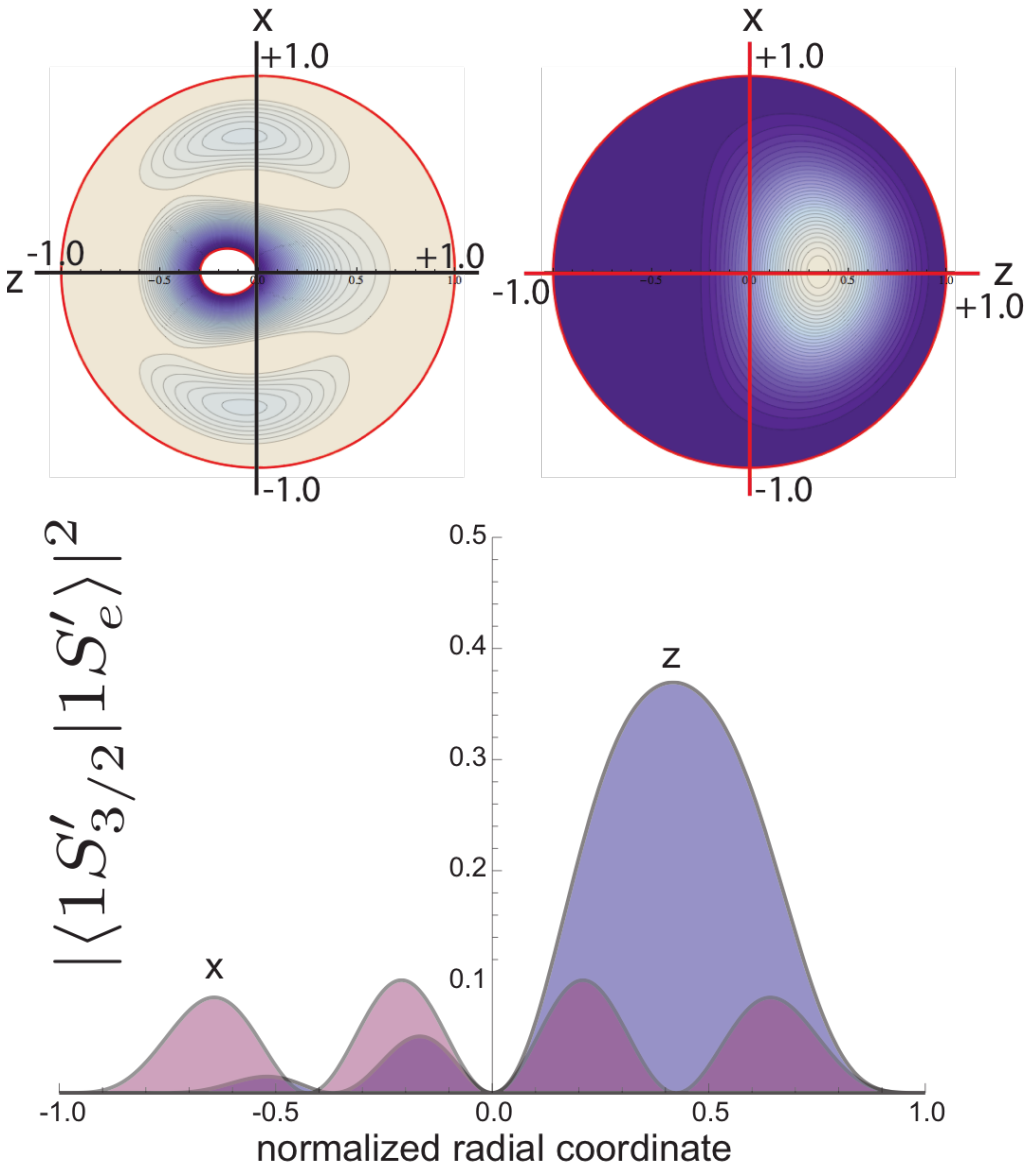

Figure 27. Normalized probability densities for hole (left) and electron (right) wavefunctions perturbed by a point (negative) charge positioned at -1 nm from the QD surface along the z-axis. The lower panel shows overlap integrals of the perturbed wavefunctions along the 'z' (blue) and 'x' (red) axes, from which we estimate a polarization ratio of ≈ 3:1.

results are similar to those reported by Wang,[84] although in our calculations the distortion of the hole state appears smaller. Physically, the distortion can be understood from a simple electrostatics argument in which the presence of a fixed charge polarizes the

electron/hole wavefunction – in addition to the change in recombination energy, the extent of that wavefunction polarization defines both the total oscillator strength and polarization properties. It is interesting to point out that *unlike* atomic or molecular transitions that accommodate angular momentum conservation via changes in orbital symmetry, light absorption/emission in quantum dots is mediated through electron-hole spin creation/annihilation thus the envelope wavefunctions for electron and holes conserve orbital symmetry.[65] In the absence of any shape or electronic perturbation, this gives rise to the so-called 2-D degenerate dipole characteristics of band-edge luminescence from quantum dots. More specifically, the optical transitions in the plane perpendicular to the c-axis of the QD involve dipole transitions $\langle 1S_e | \mu | 1S_{3/2,M=+3/2,+1/2} \rangle$ driven by right and left *circular* polarization respectively with equal probability.[10] For the perturbed wavefunctions, transition dipole matrix elements of the form $\langle 1S_e' | e \cdot z | 1S_{3/2,M=+3/2,+1/2}' \rangle$ are non-zero thus contributing to a linear polarization in emission along the z-axis. Additionally, we can look simply at the overlap functions $\left| \langle 1S_e' | 1S_{3/2,M=+3/2,+1/2}' \rangle \right| r^2 dr$ along the 'z' and 'x' axes. From this, we estimate a polarization ratio of about 3:1.

In conclusion, we have demonstrated large spectral shifts in the QD band-edge luminescence from single CdSe-OPV nanoparticles that are controlled externally by modulation of the excitation laser polarization. Supported by perturbation calculations of the magnitude of the Stark shift and resulting change in oscillator strength in the quantum dot core, these results provide compelling evidence for DC Stark effect mechanism underlying the observation of both a linear transition dipole moment and spectral shifts. We note here that the above analysis is based on a model involving the interaction of only

one polariton with the quantum dot core. In reality, the interactions between ligands and the QD in single nanostructures is more complicated, and a full treatment would require consideration of multiple, distributed ligands. Computational approaches to this problem are a matter for further investigation. These results suggest that single QDs can act as sensitive local probes of charge migration, and can be useful in both quantum dot solar cell and charge transport membranes applications.

APPENDIX A

DETERMINATION OF QUANTUM DOT C-AXIS ORIENTATION IN THE 2D DEGENERATE DIPOLE APPROXIMATION

We derived the expected probability density of modulation depths in an epi-illuminated sample of quantum dots, assuming (1) that the dots are completely spherical, and have no preference of orientation, and (2) that the transition moments of the dots are 2D degenerate in the plane perpendicular to the crystal c-axis of the nanocrystal. Again, we denote the orientation of the nanocrystal by the angular coordinates (θ, φ) made by the crystal c-axis relative to the z-axis (optic axis of the experiment, see inset of Fig. 2A). The intensity of excitation (and therefore of emission) I_{2d} as a function of (θ, φ) and the azimuthal angle of the linearly polarized excitation φ_{ex} is therefore

$$I_{2D} = I_0\left[\cos^2\theta + \sin^2\theta\cos^2(\varphi_{ex} - \varphi)\right]$$

In the course of a cycle of an anisotropy measurement, the angle φ_{ex} is swept out over 2π radians. The maximum and minimum intensity through the rotation will be

$$I_{\max} = I_0$$

and

$$I_{\min} = I_0\cos^2\theta,$$

so that the modulation depth M becomes

$$M = \frac{I_{\max} - I_{\min}}{I_{\max} + I_{\min}} = \frac{\sin^2\theta}{2 - \sin^2\theta}$$

For a uniform orientation distribution θ of the nanocrystal c-axis, we can write the differential probability P over theta (and therefore over values of modulation depth) as

$$\frac{dP}{dM} \propto \frac{d\theta}{dM} = \frac{d}{dM}\left[\sin^{-1}\sqrt{\frac{2M}{1+M}}\right]$$

$$= \frac{\sqrt{2}}{2}\frac{1}{\sqrt{1-M}}\left[\frac{1}{\sqrt{M+M^2}} - \frac{1}{1+M}\sqrt{\frac{M}{1+M}}\right].$$

Normalization gives

$$\int_0^1 \frac{d}{dM}\left[\sin^{-1}\sqrt{\frac{2M}{1+M}}\right]dM = \frac{\pi}{2}$$

so that we can write a normalized probability density over modulation depths as

$$\rho(M) = \frac{\sqrt{2}}{\pi}\frac{1}{\sqrt{1-M}}\left[\frac{1}{\sqrt{M+M^2}} - \frac{1}{1+M}\sqrt{\frac{M}{1+M}}\right].$$

By formula 3, measurement of M for a nanostructure allows determination of the c-axis orientation by

$$\theta = \sin^{-1}\sqrt{\frac{2M}{1+M}}.$$

APPENDIX B

DEFOCUSED EMISSION PATTERN IMAGING

Defocused emission pattern imaging is a technique developed by Dickson *et al.*[77, 78] to quickly deduce the orientations of molecules deposited at dielectric interfaces (i.e. glass microscope coverslips). It has been used in this group to determine the orientations of quantum dots, dendrimer cores, and organic dye molecules, both in-plane and along the optic axis. Defocused emission patterns occur as a consequence of purely classical electrodynamics. Linear organic molecules, to a very close approximation, behave as point dipoles when optically excited and emit radiation in a spatial distribution approximating a classical antenna (the so-called "sine squared" distribution). Following procedures outlined by Hellen and Axelrod[97] and Lukosz and Kunz,[98, 99] these antenna patterns are propagated through the dielectric interface and imaging optics, magnified appropriately, and finally mapped onto a pixilated image plane of the dimensions of the CCD cameras used for collection. By slightly defocusing the image, aberration of the emitted wavefront is introduced which emphasizes the optical path difference between those rays emitted along the optic axis and those emitted at high incidence angles. Comparison of the resulting image with calculated fits yields the molecular orientation. For the case of a CdSe/ZnS QD, which is often physically described as having a 2D transition dipole moment perpendicular to the crystal axis, the single point dipole is replaced by the sum of two orthogonal dipoles.

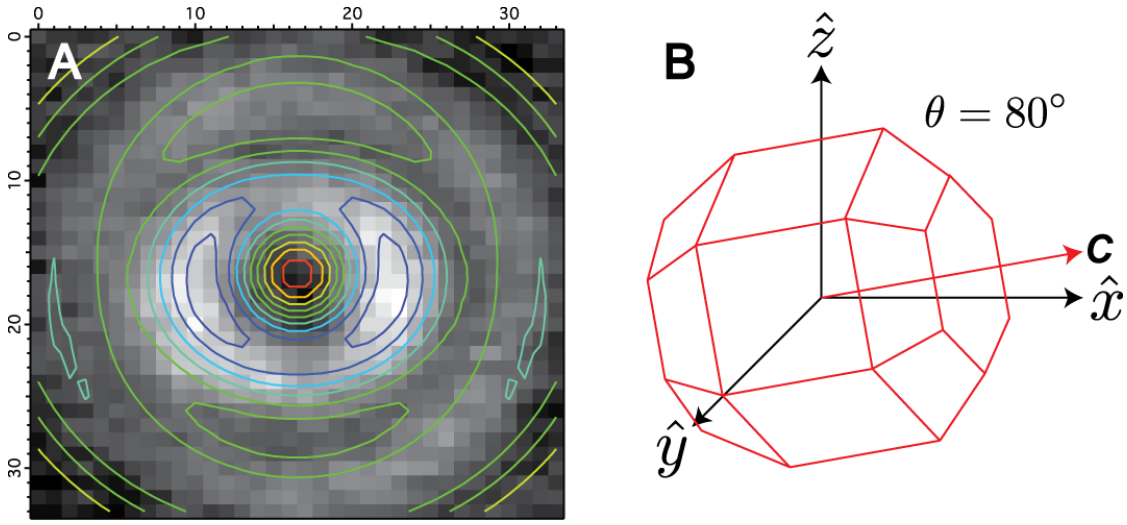

Figure B.1. (a) Experimental image (grey scale) and 2D dipole fit (contours) of a single CdSe/ZnS QD at a defocus depth of 800 nm, yielding a c-axis orientation of 80° from the optic axis. (b) Schematic representation of the nanocrystal orientation in the lab frame axis. The z-axis corresponds to the optic axis, and 'C' denotes the crystal axis. The azimuthal angle is omitted.

For common optical setups in use in our laboratory, 100X 1.4 NA objectives are used for fluorescence collection, further magnified to 400X using a telescopic expander, and imaged onto 512x512 CCD arrays with a pixel pitch of 16μm. Therefore, fluorescence images of ~ 1μm in object space correspond to ~400 μm images in image (CCD) space extending over ~ 25 pixels. Experimentally, the fluorescence signatures from single molecules and quantum dots are brought into focus, and then the objective is moved *toward* the sample plane ~600 nm. This can be achieved simply with a LabView-controlled piezo sample scanner with z-control (i.e. Physik Instrumente PINano xyz stage) connected to a multifunction DAQ board (National Instruments BNC-2110 I/O board and PCI-6221 controller). This system affords a z spatial resolution of ~10 nm. Alternatively, this can be done on a microscope outfitted with an ASI MS-2000 stage. These stages are servo-controlled and can achieve a spatial resolution of ~100 nm in the z direction. In practice, 100 nm steps in the z-direction are sufficient to differentiate between two defocus depths. Figure B.1(a) shows an experimentally-obtained defocused

image of a CdSe/ZnS QD (grey scale) overlaid with a simulated 2D dipole (contours) with a crystal tilt axis of 80° and defocus depth of 800 nm toward the sample. All other parameters are experimental values, and the QD c-axis orientation and defocus depth are determined by least-squares fit to pre-generated simulated image libraries. The physical model for the fit is shown in figure B.1(b), where the nanocrystal c-axis (denoted by *C*) is tilted by 80° relative to the optic (z) axis. Also shown is the ideal crystal structure for a hexagonal close packed (wurtzite) CdSe structure, with a C_3 symmetry axis along C. This illustrates the excellent agreement between simulated and experimental images.

There are additional criteria that must be met by the fluorescing molecule or quantum dot in order obtain defocused images. First, the emitter must be spatially fixed, either in a polymer support matrix or on a *dry* glass coverslip (residual moisture in the atmosphere can create a water film on the glass that can lead to reorientation of the molecule). Non-stationary molecules appear as a fluorescent spot that is time-averaged over many molecular orientations (if reorientation occurs on a slow enough time scale compared to data collection, subsequent images can be used to track orientational dynamics). Second, a large signal budget is required to form defocused images that can be fit, because the fluorescence photons are spread over a larger number of pixels when defocused than in aberration-free imaging conditions. This requires one or a combination of the following: (1) high pump power, (2) high fluorescence quantum yield, (3) photostable emitters, or (4) long integration times.

APPENDIX C

SINGLE QUANTUM DOT FLUORESCENCE DECAY MEASUREMENTS

We have performed extensive studies of the radiative and non-radiative decay rates of single CdSe/ZnS QDs and CdSe-OPV nanostructures. Michael Odoi, in particular, has performed a series of difficult experiments to determine the fluorescence kinetics of the hybrid organic-QD systems. These studies have included observation of an order-of-magnitude reduction in fluorescence decay times in CdSe-OPV compared to CdSe/ZnS core-shell QDs and[23] wavelength-dependent photon antibunching[100, 101] in single CdSe-OPV nanostructures.[24] By comparing the fluorescence decay rates between CdSe/ZnS QDs and CdSe-OPV nanoparticles, the role of ligands in the photoexcited exciton relaxation process have been explored in great detail. The reader is recommended to view the references cited above for more details of those measurements. In what follows, a brief description of single QD fluorescence lifetime measurements is provided.

Experimentally, CdSe/ZnS QDs are cast in nanomolar concentration from polycycloolefin polymer (Zeon Corp.) onto cleaned coverslips as described in Chapter 2. A pulsed 440 nm diode laser beam is expanded (to fill the back aperture of an objective), reflected off of a dichromatic mirror and focused onto the sample through a 1.4 NA, 100x objective. This results in a laser spot size of roughly 1000 nm in diameter. The beam is diffused to identify particles and guide them to the focus of the objective using differential stage micrometers. When this is done, the beam is refocused on a single QD. This is done to avoid excitation of multiple particles. Single QD fluorescence photons are collected back through the objective, passed through the dichromatic mirror, additionally filtered through a bandpass filter centered at the nominal QD emission wavelength (605 ±

50 nm) and focused onto the active area of avalanche photodiode (APD). The APD operates in geiger mode, sending a TTL pulse to a photon counting board (TimeHarp 200, Picoquant Gmbh.) which is also referenced to a laser sync pulse. Arrival times are binned into 4096 timing intervals with a 34 ps/bin resolution. Photon arrivals are then histogrammed into these timing bins, and the full fluorescence decay curve is constructed photon-by-photon.

Figure C.1 shows a log-normal fluorescence decay histogram of a single CdSe/ZnS QD using the apparatus described above. The pulsed laser was operated at 20 MHz repetition rate to allow the QD sufficient time to relax before the next pulse (50 ns interpulse duration). The curve is tail-fit using a single exponential function of the form

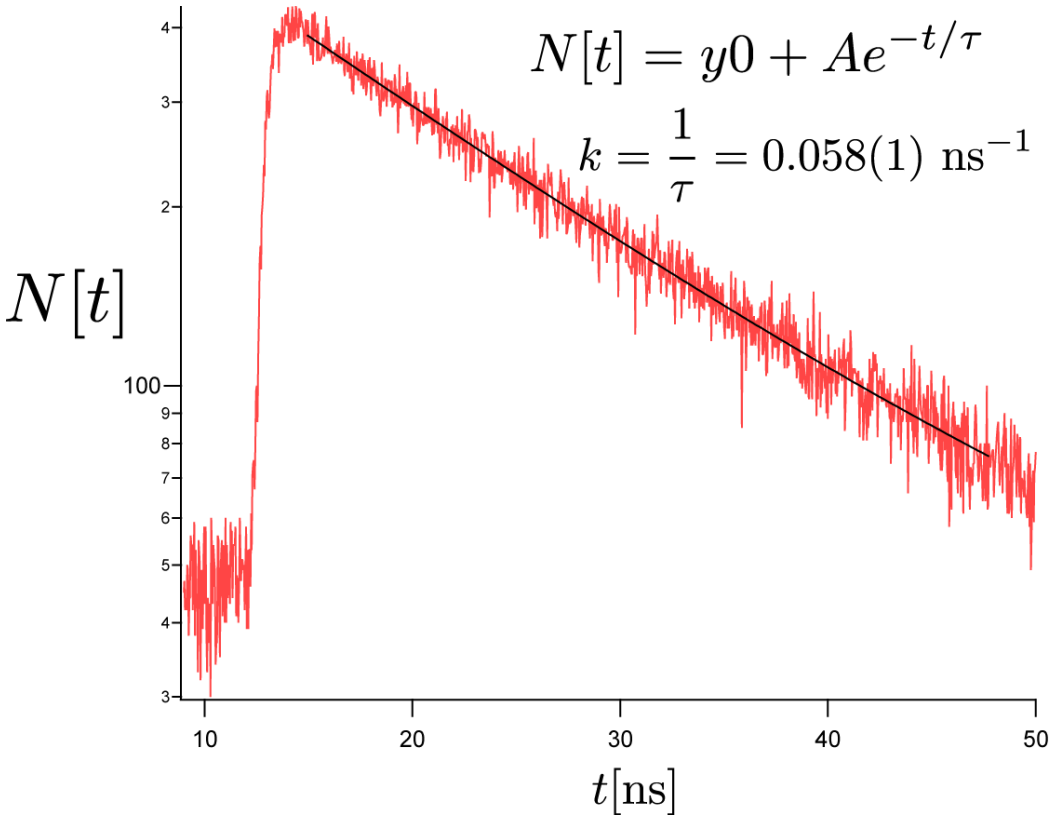

Figure C.1. Fluorescence decay histogram of a single CdSe/ZnS QD with 34 ps timing resolution. The curve is tailfit with a single exponential shown above, yielding a decay constant k = 0.058(1) ns^{-1}. This corresponds to a lifetime τ = 17.4 ns.

$$N(t) = y0 + Ae^{-t/\tau},$$

where *N(t)* is the number of photons in a given time interval *t*, *y*0 is a background offset characterizing the background noise per channel, *A* is the amplitude, and τ is the fluorescence decay time (with the decay rate k = 1/ τ). The tail fit yields $k = 0.058(1)$ ns^{-1} which corresponds to a single-QD decay lifetime of 17.4(3) ns, where the quantity in parentheses indicates the error in the last digit. Decay times on this time scale are widely reported in literature[70, 79, 102] and have been shown to fluctuate depending on emission rate.[50, 103] Rigorous fits to decay histograms require convolution of the composite instrument response function or maximum likelihood estimations; the data shown here are of sufficiently high signal-to-noise for non-rigorous tail fitting to introduce negligible error.

APPENDIX D

HOMEBUILT SAMPLE SCANNING CONFOCAL MICROSCOPE

The microscopes in our group based on inverted, research-grade microscopes are set to operate mainly in widefield imaging mode. In this mode, the samples remain stationary and images are formed on an imaging CCD with diffraction-limited resolution. Such a setup is useful for imaging on times scales above roughly 10 ms, which is limited by camera readout speed.

For experiments where both high (microsecond or nanosecond) timing resolution and spatial information are required, I built a sample scanning confocal microscope. By raster scanning a sample across a beam-waist limited excitation spot and collecting fluorescence on a point detector, intensity maps of fluorescence counts can be reconstructed. In this mode, fluorescence timing information can be stored on a TCPSC board, recovering both spatial and time-resolved information. This can be useful for many purposes (i.e. fluorescence lifetime imaging or 'FLIM') and doesn't have the disadvantage of unnecessarily photobleaching molecules, because only a very small focal volume is illuminated at any one time.

A schematic representation of the experimental setup is shown in figure D.1. A pulsed diode laser (PDL-800B) operating at 440 nm is coupled to a single mode fiber (FC), expanded to approximately 7 mm beam diameter, reflected off of a dichroic mirror (DC), and focused to a beam-waist limited laser spot using either a 100X, 1.4 NA or 1.3 NA oil-immersion, infinity-corrected objective (OBJ), resulting in a Gaussian excitation region approximately 300 nm FWHM. Samples are mounted on an XYZ piezo stage (Physik Instrumente PINano Stage). Fluorescence from the sample is collected through

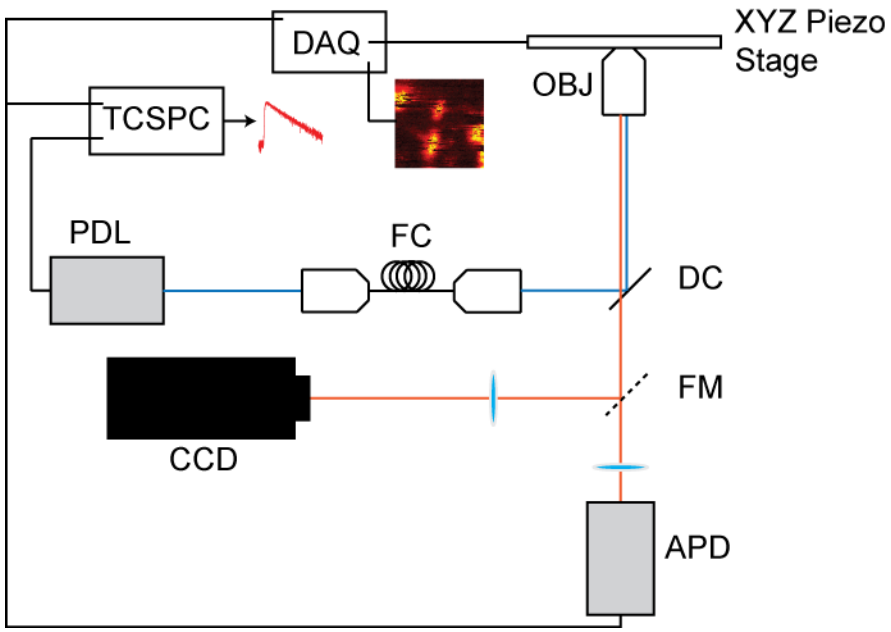

Figure D.1. Schematic of homebuilt sample scanning confocal microscope. See text for details. Abbreviations are as follows: PDL, pulsed diode laser; FC, fiber couple; DC, dichroic mirror; OBJ, objective; FM, flip mirror; APD, avalanche photodiode; CCD, charge-coupled device; TCSPC, time-correlated single photon counter; DAQ, data acquisition board.

the same objective, sent through additional laser rejection filters, and sent to either an avalanche photodiode (APD) or a CCD camera. A motorized flipper mirror directs fluorescence to either the APD or CCD for both widefield and confocal imaging capabilities. The effective confocal aperture in this experiment is the ~50 μm active area of the APD; for this reason, it is mounted on an XYZ translation stage to correctly match the z-depth of the objective. The APD operates in single photon counting mode, and counting pulses are routed to a time-correlated single photon counting (TCPSC) board and a digital counter (see below). The CCD camera is situated at the focus of a f = 500 mm achromatic doublet, resulting in an effective magnification M = 250. This camera is used primarily to check sample concentration and confirm stage coordinates.

The XYZ piezo stage is controlled by a combination of a National Instruments data acquisition board (PCI-6221) and signal access board (BNC 2110) (labeled DAQ in figure D.1). This combination is used to generate analog waveforms to control the piezo stage. A 0-10V analog signal is generated on the DAQ board using a LabView program written in-house, amplified to 0-200V using an HV amplifier (Physik Instrumente E-535.3RD), and sent to the stage to control motion in a stepwise fashion. Piezo step sizes are dictated by voltage steps (20 μm/V), allowing for steps on the order of 10 nm in X, Y, and Z dimensions and limited in practice by the analog-to-digital converter resolution. The DAQ board also has two digital input/output channels, which are configured using the same LabView program as digital counter channels. APD signals are routed to the counter and integrated over a user-defined interval and correlated to a scanner position to form a pixel-by-pixel intensity map.

Figure D.2 shows raster-scanned images of CdSe/ZnS QDs at various integration times. Figure D.2(a) shows a 10 μm confocal scan using 100 nm steps. Signal was integrated at each step for 100 ms using a software-based integrator/counter routine. Five fluorescent QDs are visible within the scan. Large streaks in the horizontal scan direction correspond to single QD blinking events, which verify that the images indeed depict photoluminescence from individual nanocrystals. The linescan in D.2(c) is a horizontal profile of the image in (a) at the set of blue lines, showing a peak fluorescence intensity of roughly 2400 counts/100ms. A Gaussian fit in blue is overlaid, with a background-

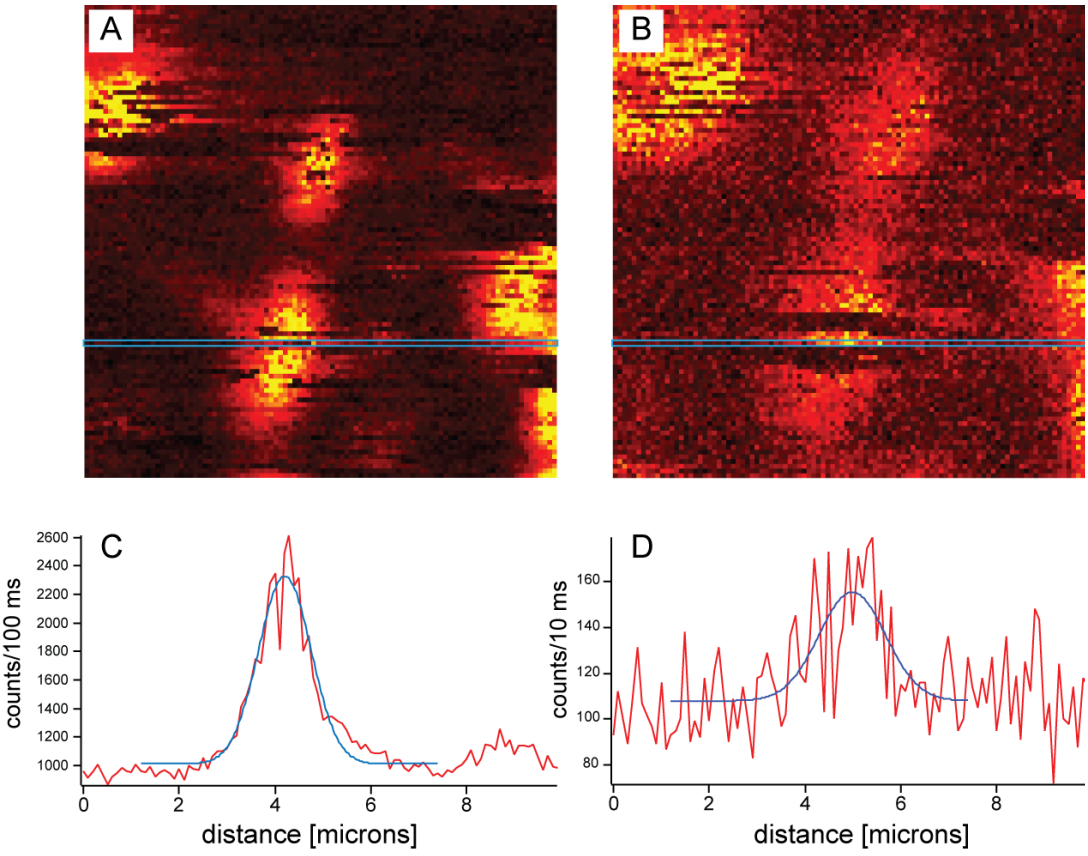

Figure D.2. (a) Confocal scan of CdSe/ZnS QDs with 100 nm step size at 100 ms integration per step. (b) Same sample scan using 10 ms integrations. (c) Line profile of the scan in (a) shown with a blue line, fitted with a Gaussian curve. (d) Line profile for the scan in (b) with a Gaussian fit.

corrected amplitude of 1315 counts and FWHM = 7.7 pixels (770 nm). The deviation from a diffraction-limited spot size is likely caused by imperfect positioning of the APD along the optic axis and extra fluorescence contributions from nearby QDs. The causes of these deviations are currently being addressed. However, it's noted here that using localization techniques described in literature,[104] the uncertainty in the spatial position of the emitter from such an image can be minimized as $\sigma \propto 1/\sqrt{N}$, where N is the integrated number of fluorescence photons in the particle spot; for the QD in the profile, this corresponds to a localization in the x-direction of less than 10 nm.

The effects of lowering integration time can be seen in figs. D.2(b) and D.2(d). These scans are taken over the same sample area as in (a), but with the integration lowered to 10ms per pixel. The signal-to-noise ratio drops significantly, which is reflected in the linescan in (d). Also apparent in the image scan is a periodic feature in the background noise; at 10ms integrations, background light from fluorescent lighting at 60 Hz (corresponding to flickering at 16ms) becomes a significant source of noise and must be well blocked.

This setup, when used in conjunction with the TCSPC electronics, allows one to construct a lifetime image by calculating a fluorescence decay time at every pixel.[105, 106] A maximum likelihood estimator (MLE) algorithm[107] can be used in cases where a small number of photons are collected at every pixel; efforts to implement this capability for this experimental setup are ongoing.

REFERENCES

1. Sivula, K.; Ball, Z. T.; Watanabe, N.; Frechet, J. M. J., Amphiphilic diblock copolymer compatibilizers and their effect on the morphology and performance of polythiophene: Fullerene solar cells. *Adv. Mater.* **2006,** *18* (2), 206-+.

2. Brabec, C. J.; Shaheen, S. E.; Fromherz, T.; Padinger, F.; Hummelen, J. C.; Dhanabalan, A.; Janssen, R. A. J.; Sariciftci, N. S., Organic photovoltaic devices produced from conjugated polymer/methanofullerene bulk heterojunctions. *Synthetic Met* **2001,** *121* (1-3), 1517-1520.

3. Coakley, K. M.; McGehee, M. D., Conjugated polymer photovoltaic cells. *Chem Mater* **2004,** *16* (23), 4533-4542.

4. Haugeneder, A.; Neges, M.; Kallinger, C.; Spirkl, W.; Lemmer, U.; Feldmann, J.; Scherf, U.; Harth, E.; Gugel, A.; Mullen, K., Exciton diffusion and dissociation in conjugated polymer fullerene blends and heterostructures. *Phys. Rev. B* **1999,** *59* (23), 15346-15351.

5. Greenham, N. C.; Peng, X. G.; Alivisatos, A. P., Charge separation and transport in conjugated-polymer/semiconductor-nanocrystal composites studied by photoluminescence quenching and photoconductivity. *Phys. Rev. B* **1996,** *54* (24), 17628-17637.

6. Huynh, W. U.; Ditmmer, J. J.; Alivisatos, P. A., Hybrid Nanorod-Polymer Solar Cells. *Science* **2002,** *295*, 2425.

7. Murray, C. B.; Norris, D. J.; Bawendi, M. G., Synthesis and Characterization of Nearly Monodisperse Cde (E = S, Se, Te) Semiconductor Nanocrystallites. *J. Am. Chem. Soc.* **1993,** *115* (19), 8706-8715.

8. Peng, X. G.; Manna, L.; Yang, W. D.; Wickham, J.; Scher, E.; Kadavanich, A.; Alivisatos, A. P., Shape control of CdSe nanocrystals. *Nature* **2000,** *404* (6773), 59-61.

9. Peng, Z. A.; Peng, X. G., Formation of high-quality CdTe, CdSe, and CdS nanocrystals using CdO as precursor. *J. Am. Chem. Soc.* **2001,** *123* (1), 183-184.

10. Efros, A. L., Luminescence Polarization of Cdse Microcrystals. *Phys. Rev. B* **1992,** *46* (12), 7448-7458.

11. Efros, A. L.; Rosen, M., The electronic structure of semiconductor nanocrystals. *Annu Rev Mater Sci* **2000,** *30*, 475-521.

12. Efros, A. L.; Rosen, M.; Kuno, M.; Nirmal, M.; Norris, D. J.; Bawendi, M., Band-edge exciton in quantum dots of semiconductors with a degenerate valence band: Dark and bright exciton states. *Phys. Rev. B* **1996,** *54* (7), 4843-4856.

13. Furis, M.; Htoon, H.; Petruska, M. A.; Klimov, V. I.; Barrick, T.; Crooker, S. A., Bright-exciton fine structure and anisotropic exchange in CdSe nanocrystal quantum dots. *Phys. Rev. B* **2006,** *73* (24), -.

14. Htoon, H.; Furis, M.; Crooker, S. A.; Jeong, S.; Klimov, V. I., Linearly polarized 'fine structure' of the bright exciton state in individual CdSe nanocrystal quantum dots. *Phys. Rev. B* **2008,** *77* (3), 035328.

15. Kittel, C., *Introduction to solid state physics*. 2nd ed.; Wiley: New York, 1956; p 617 p.

16. Alivisatos, A. P., Perspectives on the physical chemistry of semiconductor nanocrystals. *J. Phys. Chem.* **1996,** *100* (31), 13226-13239.

17. Schooss, D.; Mews, A.; Eychmuller, A.; Weller, H., Quantum-Dot Quantum-Well Cds/Hgs/Cds - Theory and Experiment. *Phys. Rev. B* **1994,** *49* (24), 17072-17078.

18. Greenham, N. C.; Peng, X. G.; Alivisatos, A. P., Charge separation and transport in conjugated polymer cadmium selenide nanocrystal composites studied by photoluminescence quenching and photoconductivity. *Synthetic Met* **1997,** *84* (1-3), 545-546.

19. Skaff, H.; Sill, K.; Emrick, T., Quantum dots tailored with poly(para-phenylene vinylene). *J. Am. Chem. Soc.* **2004,** *126* (36), 11322-11325.

20. Odoi, M. Y.; Hammer, N. I.; Sill, K.; Emrick, T.; Barnes, M. D., Observation of enhanced energy transfer in individual quantum dot-oligophenylene vinylene nanostructures. *J. Am. Chem. Soc.* **2006,** *128* (11), 3506-3507.

21. Hammer, N. I.; Early, K. T.; Sill, K.; Odoi, M. Y.; Emrick, T.; Barnes, M. D., Coverage-mediated suppression of blinking in solid state quantum dot conjugated organic composite nanostructures. *J. Phys. Chem. B* **2006,** *110* (29), 14167-14171.

22. Early, K. T.; McCarthy, K. D.; Hammer, N. I.; Odoi, M. Y.; Tangirala, R.; Emrick, T.; Barnes, M. D., Blinking suppression and intensity recurrences in single CdSe-oligo(phenylene vinylene) nanostructures: experiment and kinetic model. *Nanotechnology* **2007,** *18* (42), -.

23. Odoi, M. Y.; Hammer, N. I.; Early, K. T.; McCarthy, K. D.; Tangirala, R.; Emrick, T.; Barnes, M. D., Fluorescence lifetimes and correlated photon statistics from single CdSe/oligo(phenylene vinylene) composite nanostructures. *Nano Lett.* **2007,** *7* (9), 2769-2773.

24. Odoi, M. Y.; Early, K. T.; Tangirala, R.; Sudeep, P. K.; Emrick, T.; Barnes, M. D., Probing Multiexcitonic Emission in Single CdSe-Oligo(phenylenevinylene) Composite Nanostructures. *J. Phys. Chem. C* **2009,** *113* (31), 13462-13465.

25. Sudeep, P. K.; Early, K. T.; McCarthy, K. D.; Odoi, M. Y.; Barnes, M. D.; Emrick, T., Monodisperse oligo(phenylene vinylene) ligands on CdSe quantum dots: Synthesis and polarization anisotropy measurements. *J. Am. Chem. Soc.* **2008,** *130* (8), 2384-2385.

26. Early, K. T.; McCarthy, K. D.; Odoi, M. Y.; Sudeep, P. K.; Emrick, T.; Barnes, M. D., Linear Dipole Behavior in Single CdSe-Oligo(phenylene vinylene) Nanostructures. *Acs Nano Acs Nano* **2009,** *3* (2), 453-461.

27. Cichos, F.; von Borczyskowski, C.; Orrit, M., Power-law intermittency of single emitters. *Current Opinion in Colloid & Interface Science* **2007,** *12* (6), 272-284.

28. Efros, A. L.; Rosen, M., Random telegraph signal in the photoluminescence intensity of a single quantum dot. *Phys. Rev. Lett.* **1997,** *78* (6), 1110-1113.

29. Kuno, M.; Fromm, D. P.; Hamann, H. F.; Gallagher, A.; Nesbitt, D. J., Nonexponential "blinking" kinetics of single CdSe quantum dots: A universal power law behavior. *J. Chem. Phys.* **2000,** *112* (7), 3117-3120.

30. Kuno, M.; Fromm, D. P.; Hamann, H. F.; Gallagher, A.; Nesbitt, D. J., "On"/"off" fluorescence intermittency of single semiconductor quantum dots. *J. Chem. Phys.* **2001,** *115* (2), 1028-1040.

31. Neuhauser, R. G.; Shimizu, K. T.; Woo, W. K.; Empedocles, S. A.; Bawendi, M. G., Correlation between fluorescence intermittency and spectral diffusion in single semiconductor quantum dots. *Phys. Rev. Lett.* **2000,** *85* (15), 3301-3304.

32. Shimizu, K. T.; Neuhauser, R. G.; Leatherdale, C. A.; Empedocles, S. A.; Woo, W. K.; Bawendi, M. G., Blinking statistics in single semiconductor nanocrystal quantum dots. *Phys. Rev. B* **2001,** *6320* (20), -.

33. Antelman, J.; Ebenstein, Y.; Dertinger, T.; Michalet, X.; Weiss, S., Suppression of Quantum Dot Blinking in DTT-Doped Polymer Films. *J. Phys. Chem. C* **2009,** *113* (27), 11541-11545.

34. Hohng, S.; Ha, T., Near-complete suppression of quantum dot blinking in ambient conditions. *J. Am. Chem. Soc.* **2004,** *126* (5), 1324-1325.

35. Fomenko, V.; Nesbitt, D. J., Solution control of radiative and nonradiative lifetimes: A novel contribution to quantum dot blinking suppression. *Nano Lett.* **2008,** *8* (1), 287-293.

36. Chen, Y.; Vela, J.; Htoon, H.; Casson, J. L.; Werder, D. J.; Bussian, D. A.; Klimov, V. I.; Hollingsworth, J. A., "Giant" multishell CdSe nanocrystal quantum dots with suppressed blinking. *J. Am. Chem. Soc.* **2008,** *130* (15), 5026-+.

37. Wang, X. Y.; Ren, X. F.; Kahen, K.; Hahn, M. A.; Rajeswaran, M.; Maccagnano-Zacher, S.; Silcox, J.; Cragg, G. E.; Efros, A. L.; Krauss, T. D., Non-blinking semiconductor nanocrystals. *Nature* **2009,** *459* (7247), 686-689.

38. Nirmal, M.; Dabbousi, B. O.; Bawendi, M. G.; Macklin, J. J.; Trautman, J. K.; Harris, T. D.; Brus, L. E., Fluorescence intermittency in single cadmium selenide nanocrystals. *Nature* **1996,** *383* (6603), 802-804.

39. Klimov, V. I.; McBranch, D. W.; Leatherdale, C. A.; Bawendi, M. G., Electron and hole relaxation pathways in semiconductor quantum dots. *Phys. Rev. B* **1999,** *60* (19), 13740-13749.

40. Frantsuzov, P. A.; Marcus, R. A., Explanation of quantum dot blinking without the long-lived trap hypothesis. *Phys. Rev. B* **2005,** *72* (15), -.

41. Jung, Y.; Barkai, E.; Silbey, R. J., Lineshape theory and photon counting statistics for blinking quantum dots: a Levy walk process. *Chem. Phys.* **2002,** *284* (1-2), 181-194.

42. Margolin, G.; Barkai, E., Aging correlation functions for blinking nanocrystals, and other on-off stochastic processes. *J. Chem. Phys.* **2004,** *121* (3), 1566-1577.

43. Margolin, G.; Barkai, E., Nonergodicity of blinking nanocrystals and other Levy-walk processes. *Phys. Rev. Lett.* **2005,** *94* (8), -.

44. Sanford, S.; Voura, E.; Jaiswal, J.; Mattoussi, H., Spectral imaging of quantum dots in mice. *J Histochem Cytochem* **2004,** *52*, S19-S19.

45. Voura, E. B.; Jaiswal, J. K.; Mattoussi, H.; Simon, S. M., Tracking metastatic tumor cell extravasation with quantum dot nanocrystals and fluorescence emission-scanning microscopy. *Nat Med* **2004,** *10* (9), 993-998.

46. Brokmann, X.; Giacobino, E.; Dahan, M.; Hermier, J. P., Highly efficient triggered emission of single photons by colloidal CdSe/ZnS nanocrystals. *Appl. Phys. Lett.* **2004,** *85* (5), 712-714.

47. Verberk, R.; van Oijen, A. M.; Orrit, M., Simple model for the power-law blinking of single semiconductor nanocrystals. *Phys. Rev. B* **2002,** *66* (23), -.

48. Brokmann, X.; Hermier, J. P.; Messin, G.; Desbiolles, P.; Bouchaud, J. P.; Dahan, M., Statistical aging and nonergodicity in the fluorescence of single nanocrystals. *Phys. Rev. Lett.* **2003,** *90* (12), -.

49. Verberk, R.; Chon, J. W. M.; Gu, M.; Orrit, M., Environment-dependent blinking of single semiconductor nanocrystals and statistical aging of ensembles. *Physica E* **2005,** *26* (1-4), 19-23.

50. Biebricher, A.; Sauer, M.; Tinnefeld, P., Radiative and nonradiative rate fluctuations of single colloidal semiconductor nanocrystals. *J. Phys. Chem. B* **2006,** *110* (11), 5174-5178.

51. Empedocles, S. A.; Norris, D. J.; Bawendi, M. G., Photoluminescence spectroscopy of single CdSe nanocrystallite quantum dots. *Phys. Rev. Lett.* **1996,** *77* (18), 3873-3876.

52. Koberling, F.; Mews, A.; Basche, T., Oxygen-induced blinking of single CdSe nanocrystals. *Adv. Mater.* **2001,** *13* (9), 672-676.

53. Ray, K.; Badugu, R.; Lakowicz, J. R., Metal-enhanced fluorescence from CdTe nanocrystals: A single-molecule fluorescence study. *J. Am. Chem. Soc.* **2006,** *128* (28), 8998-8999.

54. Bergquist, J. C.; Hulet, R. G.; Itano, W. M.; Wineland, D. J., Observation of Quantum Jumps in a Single Atom. *Phys. Rev. Lett.* **1986,** *57* (14), 1699-1702.

55. Cook, R. J.; Kimble, H. J., Possibility of Direct Observation of Quantum Jumps. *Phys. Rev. Lett.* **1985,** *54* (10), 1023-1026.

56. Tang, J.; Marcus, R. A., Mechanisms of fluorescence blinking in semiconductor nanocrystal quantum dots. *J. Chem. Phys.* **2005,** *123* (5), -.

57. Tang, J.; Marcus, R. A., Diffusion-controlled electron transfer processes and power-law statistics of fluorescence intermittency of nanoparticles. *Phys. Rev. Lett.* **2005,** *95* (10), -.

58. Pelton, M.; Smith, G.; Scherer, N. F.; Marcus, R. A., Evidence for a diffusion-controlled mechanism for fluorescence blinking of colloidal quantum dots. *P Natl Acad Sci USA* **2007,** *104* (36), 14249-14254.

59. Empedocles, S. A.; Bawendi, M. G., Influence of spectral diffusion on the line shapes of single CdSe nanocrystallite quantum dots. *J. Phys. Chem. B* **1999,** *103* (11), 1826-1830.

60. Tang, J.; Marcus, R. A., Determination of energetics and kinetics from single-particle intermittency and ensemble-averaged fluorescence intensity decay of quantum dots. *J. Chem. Phys.* **2006,** *125* (4), -.

61. Shimizu, K. T.; Woo, W. K.; Fisher, B. R.; Eisler, H. J.; Bawendi, M. G., Surface-enhanced emission from single semiconductor nanocrystals. *Phys. Rev. Lett.* **2002,** *89* (11), -.

62. Pokrant, S.; Whaley, K. B., Tight-binding studies of surface effects on electronic structure of CdSe nanocrystals: the role of organic ligands, surface reconstruction, and inorganic capping shells. *Eur. Phys. J. D* **1999,** *6* (2), 255-267.

63. Izrailev, F. M.; Castaneda-Mendoza, A., Return probability: Exponential versus Gaussian decay. *Phys. Lett. A* **2006,** *350* (5-6), 355-362.

64. Chowdhury, A.; Yu, L. P.; Raheem, I.; Peteanu, L.; Liu, L. A.; Yaron, D. J., Stark spectroscopy of size-selected helical H-aggregates of a cyanine dye templated by duplex DNA. Effect of exciton coupling on electronic polarizabilities. *J. Phys. Chem. A* **2003,** *107* (18), 3351-3362.

65. Efros, A. L.; Rodina, A. V., Band-Edge Absorption and Luminescence of Nonspherical Nanometer-Size Crystals. *Phys. Rev. B* **1993,** *47* (15), 10005-10007.

66. Nirmal, M.; Norris, D. J.; Kuno, M.; Bawendi, M. G.; Efros, A. L.; Rosen, M., Observation of the Dark Exciton in Cdse Quantum Dots. *Phys. Rev. Lett.* **1995,** *75* (20), 3728-3731.

67. Chung, I. H.; Shimizu, K. T.; Bawendi, M. G., Room temperature measurements of the 3D orientation of single CdSe quantum dots using polarization microscopy. *P Natl Acad Sci USA* **2003,** *100* (2), 405-408.

68. Empedocles, S. A.; Neuhauser, R.; Bawendi, M. G., Three-dimensional orientation measurements of symmetric single chromophores using polarization microscopy. *Nature* **1999,** *399* (6732), 126-130.

69. Bohmer, M.; Enderlein, J., Orientation imaging of single molecules by wide-field epifluorescence microscopy. *J. Opt. Soc. Am. B* **2003,** *20* (3), 554-559.

70. Brokmann, X.; Coolen, L.; Hermier, J. P.; Dahan, M., Emission properties of single CdSe/ZnS quantum dots close to a dielectric interface. *Chem. Phys.* **2005,** *318* (1-2), 91-98.

71. Patra, D.; Gregor, I.; Enderlein, J.; Sauer, M., Defocused imaging of quantum-dot angular distribution of radiation. *Appl. Phys. Lett.* **2005,** *87* (10), 101103.

72. Schuster, R.; Barth, M.; Gruber, A.; Cichos, F., Defocused wide field fluorescence imaging of single CdSe/ZnS quantum dots. *Chem. Phys. Lett.* **2005,** *413* (4-6), 280-283.

73. Ha, T.; Enderle, T.; Chemla, D. S.; Selvin, P. R.; Weiss, S., Single molecule dynamics studied by polarization modulation. *Phys. Rev. Lett.* **1996,** *77* (19), 3979-3982.

74. Ha, T.; Laurence, T. A.; Chemla, D. S.; Weiss, S., Polarization spectroscopy of single fluorescent molecules. *J. Phys. Chem. B* **1999,** *103* (33), 6839-6850.

75. Macklin, J. J.; Trautman, J. K.; Harris, T. D.; Brus, L. E., Imaging and time-resolved spectroscopy of single molecules at an interface. *Science* **1996,** *272* (5259), 255-258.

76. Bartko, A. P.; Dickson, R. M., Imaging three-dimensional single molecule orientations. *J. Phys. Chem. B* **1999,** *103* (51), 11237-11241.

77. Dickson, R. M.; Norris, D. J.; Moerner, W. E., Simultaneous imaging of individual molecules aligned both parallel and perpendicular to the optic axis. *Phys. Rev. Lett.* **1998,** *81* (24), 5322-5325.

78. Dickson, R. M.; Norris, D. J.; Tzeng, Y. L.; Moerner, W. E., Three-dimensional imaging of single molecules solvated in pores of poly(acrylamide) gels. *Science* **1996,** *274* (5289), 966-969.

79. Brokmann, X.; Coolen, L.; Dahan, M.; Hermier, J. P., Measurement of the radiative and nonradiative decay rates of single CdSe nanocrystals through a controlled modification of their spontaneous emission. *Phys. Rev. Lett.* **2004,** *93* (10), -.

80. Ginger, D. S.; Greenham, N. C., Photoinduced electron transfer from conjugated polymers to CdSe nanocrystals. *Phys. Rev. B* **1999,** *59* (16), 10622-10629.

81. Jackson, J. D., *Classical electrodynamics*. 3rd ed.; Wiley: New York, 1999; p xxi, 808 p.

82. Guyot-Sionnest, P.; Wehrenberg, B.; Yu, D., Intraband relaxation in CdSe nanocrystals and the strong influence of the surface ligands. *J. Chem. Phys.* **2005,** *123* (7), 074709.

83. Empedocles, S. A.; Bawendi, M. G., Quantum-confined stark effect in single CdSe nanocrystallite quantum dots. *Science* **1997,** *278* (5346), 2114-2117.

84. Wang, L. W., Calculating the influence of external charges on the photoluminescence of a CdSe quantum dot. *J. Phys. Chem. B* **2001,** *105* (12), 2360-2364.

85. Hu, J. T.; Li, L. S.; Yang, W. D.; Manna, L.; Wang, L. W.; Alivisatos, A. P., Linearly polarized emission from colloidal semiconductor quantum rods. *Science* **2001,** *292* (5524), 2060-2063.

86. Milliron, D. J.; Alivisatos, A. P.; Pitois, C.; Edder, C.; Frechet, J. M. J., Electroactive surfactant designed to mediate electron transfer between CdSe nanocrystals and organic semiconductors. *Adv. Mater.* **2003,** *15* (1), 58-61.

87. Jung, C.; Hellriegel, C.; Platschek, B.; Wohrle, D.; Bein, T.; Michaelis, J.; Brauchle, C., Simultaneous measurement of orientational and spectral dynamics of single molecules in nanostructured host-guest materials. *J. Am. Chem. Soc.* **2007,** *129* (17), 5570-5579.

88. Muller, J.; Lupton, J. M.; Rogach, A. L.; Feldmann, J.; Talapin, D. V.; Weller, H., Monitoring surface charge migration in the spectral dynamics of single CdSe/CdS nanodot/nanorod heterostructures. *Phys. Rev. B* **2005,** *72* (20), 205339.

89. Biadala, L.; Louyer, Y.; Tamarat, P.; Lounis, B., Direct Observation of the Two Lowest Exciton Zero-Phonon Lines in Single CdSe/ZnS Nanocrystals. *Phys. Rev. Lett.* **2009,** *103* (3), 37404.

90. Shen, Y. M.; Pang, L.; Fainman, Y.; Griswold, M.; Yang, S.; Butov, L. V.; Sham, L. J., Photoluminescence spectral switching of single CdSe/ZnS colloidal nanocrystals in poly(methyl methacrylate). *Phys. Rev. B* **2007,** *76* (8), 085312.

91. Lee, S. F.; Osborne, M. A., Brightening, Blinking, Bluing and Bleaching in the Life of a Quantum Dot: Friend or Foe? *Chemphyschem* **2009,** *10* (13), 2174-2191.

92. van Sark, W. G. J. H. M.; Frederix, P. L. T. M.; Bol, A. A.; Gerritsen, H. C.; Meijerink, A., Blueing, bleaching, and blinking of single CdSe/ZnS quantum dots. *Chemphyschem* **2002,** *3* (10), 871-879.

93. Empedocles, S. A.; Neuhauser, R.; Shimizu, K.; Bawendi, M. G., Photoluminescence from single semiconductor nanostructures. *Adv. Mater.* **1999,** *11* (15), 1243-1256.

94. Campbell, I. H.; Hagler, T. W.; Smith, D. L.; Ferraris, J. P., Direct measurement of conjugated polymer electronic excitation energies using metal/polymer/metal structures. *Phys. Rev. Lett.* **1996,** *76* (11), 1900-1903.

95. Ginger, D. S.; Greenham, N. C., Charge separation in conjugated-polymer/nanocrystal blends. *Synthetic Met* **1999,** *101* (1-3), 425-428.

96. Wang, L. W.; Zunger, A., Pseudopotential calculations of nanoscale CdSe quantum dots. *Phys. Rev. B* **1996,** *53* (15), 9579-9582.

97. Hellen, E. H.; Axelrod, D., Fluorescence Emission at Dielectric and Metal-Film Interfaces. *J. Opt. Soc. Am. B* **1987,** *4* (3), 337-350.

98. Lukosz, W.; Kunz, R. E., Light-Emission by Magnetic and Electric Dipoles Close to a Plane Interface .1. Total Radiated Power. *J Opt Soc Am* **1977,** *67* (12), 1607-1615.

99. Kunz, R. E.; Lukosz, W., Light-Emission of Electric and Magnetic Dipoles in Region of Dielectric Interface. *Helv Phys Acta* **1977,** *50* (5), 657-657.

100. Mandel, H. J. K.; Dagenais, M.; L., Photon Antibunching in Resonance Fluorescence. *Phys. Rev. Lett.* **1977,** *39* (11), 4.

101. Walls, D. F.; Milburn, G. J.; SpringerLink (Online service), Quantum Optics. Springer-Verlag Berlin Heidelberg: Berlin, Heidelberg, 2008.

102. Fisher, B. R.; Eisler, H. J.; Stott, N. E.; Bawendi, M. G., Emission intensity dependence and single-exponential behavior in single colloidal quantum dot fluorescence lifetimes. *J. Phys. Chem. B* **2004,** *108* (1), 143-148.

103. Zhang, K.; Chang, H. Y.; Fu, A. H.; Alivisatos, A. P.; Yang, H., Continuous distribution of emission states from single CdSe/ZnS quantum dots. *Nano Lett.* **2006,** *6* (4), 843-847.

104. Thompson, R. E.; Larson, D. R.; Webb, W. W., Precise nanometer localization analysis for individual fluorescent probes. *Biophys J* **2002,** *82* (5), 2775-2783.

105. Becker, W.; Bergmann, A.; Borst, J. W.; Hink, M. A.; Visser, A. J. W. G., High resolution FLIM combined with FCS in a single laser scanning microscope. *Biophys J* **2003,** *84* (2), 313A-313A.

106. Lin, H. J.; Herman, P.; Lakowicz, J. R., FLIM: A way to image pH distribution in living cells. *Biophys J* **2001,** *80* (1), 367A-367A.

107. Tellinghuisen, J.; Wilkerson, C. W., Bias and Precision in the Estimation of Exponential Decay Parameters from Sparse Data. *Anal Chem* **1993,** *65* (9), 1240-1246.